Journal of the Meteorological Society of Japan, Vol. 88, No. 2, pp. 95–121, 2010.
DOI:10.2151/jmsj.2010-201

Evaluation of an Explicit One-Dimensional Time Dependent Tilting Cloud Model: Sensitivity to Relative Humidity

Shu-Hua CHEN

Department of Land, Air, and Water Resources, University of California, Davis, California, USA
Department of Atmospheric Sciences, National Central University, Chung-Li, Taiwan

and

Yang-Cheng SIAO

Department of Atmospheric Sciences, National Central University, Chung-Li, Taiwan

(Manuscript received 19 January 2009, in final form 4 November 2009)

Abstract

The primary goal of this study is to evaluate the performance of the Explicit One-dimensional (1D) Time-dependent Tilting Cloud Model (ETTM), which will be potentially used in a cumulus parameterization scheme. The Weather Research and Forecasting (WRF) model was used in a cloud-resolving mode to study 3D cloud characteristics under two sheared environments, one from the Rain in Cumulus over the Ocean (RICO) field experiment and the other from the International H_2O Project (IHOP). Then, WRF 3D simulation results were used to evaluate ETTM performance. WRF simulations were performed with different radii from 1 km to 10 km of thermal bubbles for initiation. The three-dimensional cloud features were quite different between RICO and IHOP due to their environments, which were sub-tropical maritime sounding and mid-latitude continental sounding, respectively. ETTM 1D cloud simulations, corresponding to each of the WRF simulations, were conducted. The simulated 1D clouds were too weak when the original thermal bubbles were similar to those used in the 3D cloud simulations (i.e., no additional moisture within the thermal bubbles). The sensitivity of model results to relative humidity was tested by imposing a lower bound of 88% (ER88) and 95% (ER95) humidity to the thermal bubble in ETTM simulations. When compared with the original simulations, 1D results from ER88 and ER95 showed clear improvements, but they were still underestimated relative to 3D clouds, and the results from IHOP were slightly worse than those from RICO. Sensitivity tests with a zero-degree cloud tilting angle and with a different radius of the downdraft were also examined. Results show that the downdraft due to the tilting of the cloud slightly improved ETTM's performance in terms of the heat and moisture fluxes, while the influence of using different downdraft sizes on 1D simulation results is not clear.

1. Introduction

The purposes of cumulus parameterization are to estimate unresolved subgrid-scale precipitation; to account for subgrid scale latent heat release; and to vertically redistribute heat, moisture, and momentum (Kain and Fritsch 1993). Even though advances in computational resources and techniques make it possible to run global cloud-resolving models, they are mostly available at a few national centers such as the Earth Simulator at the Japan Agency for Marine-Earth Science and Technology (JAMSTEC). Therefore, cumulus parameterization in numerical models is and will still be needed, particularly for long-term global climate integrations,

Corresponding author: Shu-Hua Chen, Department of Land, Air, and Water Resources, University of California, Davis, California 95616-8627, USA.
E-mail: shachen@ucdavis.edu

for most research institutes. The importance of the cumulus representation cannot be over-emphasized as errors in moist physics schemes overwhelm those in dynamics.

In general, cumulus parameterization consists of three components: triggering functions, which manage the timing and location of subgrid-scale convection; the vertical redistribution of mass, momentum, heat, and moisture variables, which control the modification of the grid-scale environment; and closure assumptions, which regulate the strength of the convection. Arakawa (2004) provided a very comprehensive review of the history of cumulus parameterization. Different cumulus parameterizations, in particular, the moist-convective adjustment scheme (Manabe et al. 1965), the Kuo scheme (Kuo 1974), and the Arakawa scheme (Arakawa 1969), were reviewed. The controversies, current trends, and outstanding problems of cumulus parameterization were also discussed.

Following the improvement of computational resources, a 2D cloud model was used in each model grid column to directly resolve subgrid-scale clouds to provide the vertical distribution of mass and other cloud-related properties (i.e., eliminating the triggering function and the closure assumption) (Grabowski 2001), known as the super parameterization scheme. Results from the super parameterization scheme were very promising, and its application has been expanded (Khairoutdinov et al. 2005; Khairoutdinov et al. 2008; Tao et al. 2008). However, it is not without weaknesses. For example, this scheme modeled extensive rainfall in the western Pacific during the Northern Hemisphere summer (Khairoutdinov et al. 2005). Additionally, the super parameterization scheme requires about two orders of magnitude more computational time than the conventional cumulus parameterization approach, as a 2D cloud model is calculated in each model grid box during the entire model integration (Khairoutdinov et al. 2005). Therefore, there are obstacles to the widespread adoption of the super parameterization scheme, particularly for those with limited computer resources, in which case cumulus parameterization by a 1D cloud model might be more practical.

Most of the 1D cloud models that are used in cumulus parameterization are either simple plumes or bulk 1D cloud models (e.g., Anthes 1977; Fritsch and Chappell 1980; Frank and Cohen 1985; Grell 1993; Hu 1997), which might not perform properly due to their simplifications (Liu et al. 2001). A slightly more sophisticated 1D entrainment/detrainment plume model was then proposed by Kain and Fritsch (1990, 1993) and a more realistic 1D model was developed by Haines and Sun (1994) for cumulus parameterization. All these 1D models are time independent and some of them ignore downdraft effects. The importance of the downdraft to cumulus parameterization has been suggested by many researchers (Brown 1979; Molinari and Corsetti 1985; Cheng 1989; Grell et al. 1991; Moncrieff 1992; Gray 2000; Liu et al. 2001). Downdrafts, which are often observed beside tilted updrafts, have non-negligible effects on the mass, moisture, and heat fluxes at low levels (Moncrieff 1981, 1992). As pointed out in Grell et al. (1991), a more realistic 1D model such as the one that is time-dependent and physically based might be needed in order to obtain a better estimate of the subgrid-scale thermodynamic properties of clouds in cumulus parameterization. Ferrier and Houze (1989) developed a time-dependent 1D model, which included relatively complete physical processes. In their model, the precipitation separating from the updraft due to its tilting effect was also considered; however, the downdraft initiated by the evaporative/sublimation/melting cooling and the drag force was ignored.

Chen and Sun (2004) developed an Explicit One-dimensional Time-dependent Tilting Cloud Model (ETTM) for potential use in cumulus parameterization. A brief introduction to the model is given in Section 2.2. Before applying ETTM to a cumulus parameterization scheme, it is important to evaluate the model performance under realistic environments. Cloud resolving models (CRMs) have been used to study three-dimensional (3D) or two-dimensional (2D) cloud properties (Lin 1999; Murata and Ueno 2005; Gao and Li 2008; Luo et al. 2008) and applied to validate the performance of cumulus parameterization schemes (Liu et al. 2001). In this study, the weather research and forecasting (WRF) model was used in a cloud-resolving mode to study 3D cloud properties under different shear and convective available potential energy (CAPE) environments. The results from WRF were then used to evaluate and improve ETTM's performance.

This paper is organized as follows. Both models, 3D WRF and 1D ETTM, and the initial soundings are introduced in Section 2. WRF model experiment designs and simulation results are given in Section 3, while those of ETTM simulations and comparisons between the two model results are presented in Section 4. Brief concluding remarks are given in Section 5.

2. Brief description of models and initial soundings

2.1 *The weather research and forecasting (WRF) model*

WRF is a community model recently developed by several organizations. There are two dynamical cores available for the public: the Advanced Research WRF (ARW) and the Nonhydrostatic Mesoscale Model (NMM). The ARW version 2.2 (Skamarock et al. 2005) was adopted for this study. ARW is a fully compressible, nonhydrostatic model, and the governing equations are written in flux form to conserve mass, dry entropy, and scalars. The Runge-Kutta third-order time scheme was employed and the fifth- and third-order advection schemes were chosen for the horizontal and vertical directions, respectively. An open lateral boundary condition was used, and the surface fluxes were deactivated. WRF was designed to help researchers develop and study advanced physics and data assimilation systems, and it can be used for both idealized and real case studies. In this study WRF was adopted as a cloud-resolving model (CRM) for semi-idealized 3D cloud simulations, which used real soundings with an idealized model setting (e.g., horizontally homogeneous initial conditions).

2.2 *Explicit one-dimensional time-dependent tilting cloud model (ETTM)*

ETTM was developed by Chen and Sun (2004) for potential use in cumulus parameterization. ETTM includes several important features: the cloud can tilt; an updraft and a downdraft can coexist; a sophisticated cloud microphysics is used; and the model is anelastic, non-hydrostatic, and time-dependent. The cloud microphysics scheme of ETTM (Chen and Sun 2002) is one of the microphysics schemes available in the WRF model (e.g., the Purdue Lin microphysics scheme). Therefore, WRF is one of the most suitable models for comparing ETTM results with 3D cloud simulations.

The ETTM model includes three 1D columns in calculation: the updraft, downdraft, and environment. The first two columns are time dependent, while the third (i.e., environment) is assumed to be time-independent. All three columns are initialized with the same sounding. The updraft is activated by a (moist) thermal bubble, while the downdraft is triggered by evaporative/sublimation cooling of detrained hydrometeors and by the drag force as well as the melting effect (i.e., snow and graupel) of separated precipitation from the updraft (Fig. 1). Note that in ETTM all downdrafts are considered as a single entity the ones due to separated precipitation and the ones due to detrained hydrometeors in. As in WRF simulations, no surface flux was assumed.

In ETTM, two parameters were introduced, the cloud radius (R) and the tilting angle (α_o). The tilting angle, which was assumed to be the same for both updraft and downdraft, was defined as the angle from the vertical axis in erect cylindrical coordinates to the tilting axis in tilting cylindrical coordinates. The cloud radius of the downdraft

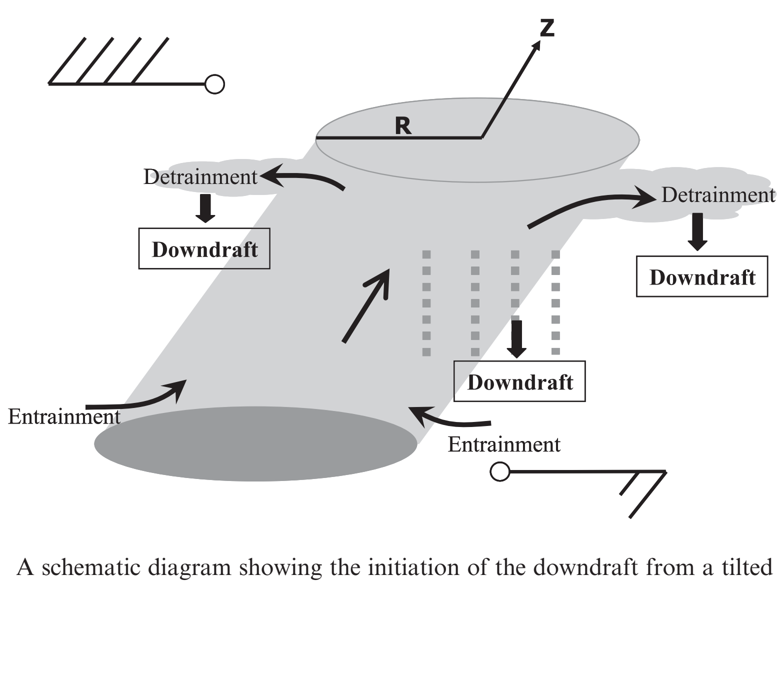

Fig. 1. A schematic diagram showing the initiation of the downdraft from a tilted updraft.

was assumed to be 40% of that for the updraft; this assumption was based on the study by Lemone and Zipser (1980). Although the cloud radius and tilting angle are functions of time, they were assumed to be constant in the ETTM model for simplicity. Both parameters were estimated from three dimensional clouds in this study and will be parameterized in the near future.

2.3 Soundings

Both WRF and ETTM were initialized with the same vertical soundings. In WRF, it was assumed that the initial fields were horizontally homogeneous. Two real 1D environmental soundings (Fig. 2 and Table 1) were used for this semi-idealized study. One is from the Rain in Cumulus over the Ocean (RICO) field experiment and the other is from the International H_2O Project (IHOP). The sounding from RICO was observed at 0000 UTC December 18, 2004 from San Juan, Puerto Rico, a sub-tropical environment where the low levels were moist (Fig. 2a). The horizontal winds changed from easterly-southeasterly near the surface to westerly-northwesterly as the height increased (Fig. 2c), giving an approximately normal unidirectional shear with height. Although the convective available potential energy (CAPE) was sufficiently large (1400 J kg^{-1}), only a few scattered clouds were observed around Puerto Rico during the day on December 18, 2004.

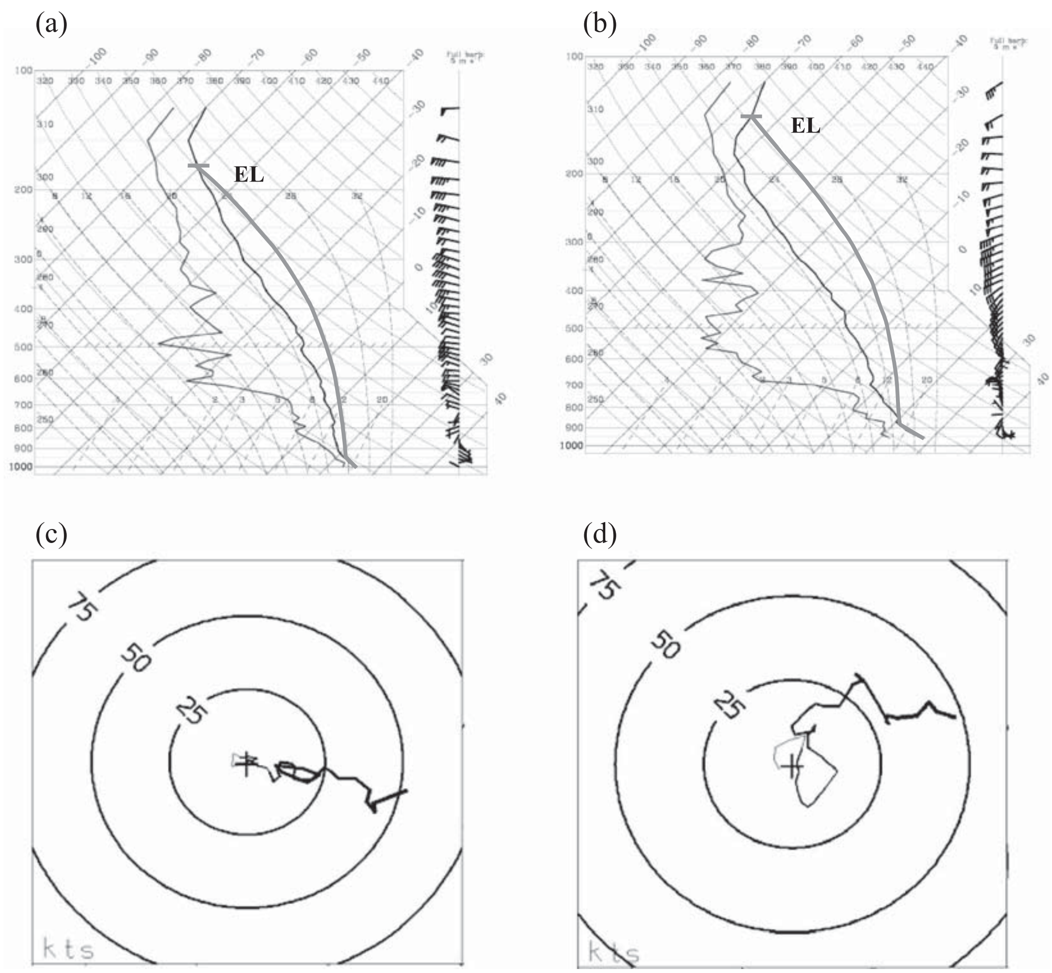

Fig. 2. The soundings used for (a) RICO and (b) IHOP simulations. The thick gray curve in (a) and (b) presents the dry and then moist adiabatic processes for an air parcel that was lifted upward from the surface. EL stands for the equilibrium level; (c) and (d) are hodographs of (a) and (b), respectively, from the surface to 500 hPa.

Table 1. Information for the two soundings that were used in this study.

	Sounding 1	Sounding 2
Field Experiment	RICO	IHOP
Station	SJU San Juan, Puerto Rico	OUN Norman, Oklahoma, USA
Latitude/Longitude	−66.0°/18.4°	−97.40°/35.20°
Observed time	0000 UTC December 18, 2004	2100 UTC June 4, 2002
Convective Available Potential Energy	~1400 J kg^{-1}	~2450 J kg^{-1}
Deducted mean wind U (m s^{-1}), v (m s^{-1})	−5.9, −2.5	−1.17, 5.76

The sounding from IHOP was collected at 2100 UTC June 4, 2002, and it was a sounding from the Great Plains of the US, in the continental middle latitudes, where the low levels were relatively dry (Fig. 2b). For IHOP, in addition to a drier lower atmosphere, the CAPE was larger (2450 J kg^{-1}) than that from RICO (1400 J kg^{-1}) and the wind shear direction changed with height, i.e., multi-directional shear (Fig. 2c vs. 2d). At 0000 UTC June 4, 2002, there was a linear convective system (squall line) propagating from the northwestern direction toward the city of Norman, OK, where the sounding was measured. For both soundings, the temperature profiles were close to dry adiabatic at low levels and approached a moist adiabatic structure in the middle levels. However, the dry adiabatic-like lower atmosphere was much deeper in IHOP than in RICO. As a result, the temperature for IHOP dropped by about 20 K from the surface to 700 hPa, which was more than the temperature drop observed for RICO (about 16 K).

3. WRF simulations

3.1 Experiment design

The idealized supercell case in the WRF model was adopted for semi-idealized 3D simulations. As mentioned earlier, the initial fields were assumed horizontally homogeneous and two case simulations, RICO and IHOP, were conducted using the soundings in Fig. 2. One domain with $321 \times 321 \times 51$ grid points in the east–west, north–south, and vertical directions, respectively, was configured for all the WRF simulations. The horizontal resolution was 250 m, which gave a horizontal domain size of 80 km × 80 km. The vertical grids were stretched from a resolution of approximately 200 m close to the surface to 1000 m close to the model top at approximately 16-km height. A weakly-damped 5-km Rayleigh sponge layer was placed at the top of the domain to absorb reflected waves. The damping effect quickly decreased downward. Because of the high spatial resolution, a subgrid eddy diffusion scheme, the Smagorinsky scheme (Smagorinsky 1963), was used in place of boundary layer parameterization. The Purdue Lin microphysics scheme (Chen and Sun 2002) was chosen, as mentioned earlier, and a free-slip boundary lower condition was used.

The 3D cloud simulation was initiated using a thermal bubble. For both RICO and IHOP, simulations with different horizontal radii of bubbles were conducted to examine cloud properties with different cloud sizes. A maximum potential temperature perturbation ($\theta'_{\max}$) of 3 K was assigned at the center of the bubble. The formula of the thermal bubble (θ') was:

$$\theta' = \theta'_{\max} \times \cos^2(\pi r/2), \tag{1}$$

where $r = \sqrt{\left(\frac{x-x_o}{R}\right)^2 + \left(\frac{y-y_o}{R}\right)^2 + \left(\frac{z-z_o}{1500}\right)^2}$.

The center of the bubble, (x_o, y_o, z_o), was located at a 1.5 km height over the center of the model domain. The bubble radius R varied from 2 km to 10 km for RICO and 3 km to 10 km for IHOP, with an interval of 1 km. Simulations with smaller bubble radii (i.e., 1 km for RICO and 1–2 km for IHOP) were also examined but not included because their simulated cloud diameters were less than five grid spacings (i.e., less than 1.25 km). The model was integrated for 1 h with a time step of 1 s. Note that in order to keep the simulated storms close to the center of the domain, mean winds of $(u, v) = (-5.9 \text{ m s}^{-1}, -2.5 \text{ m s}^{-1})$ for RICO and $(u, v) = (-1.17 \text{ m s}^{-1}, 5.76 \text{ m s}^{-1})$ for IHOP were deducted from the initial soundings. The mean wind was estimated from the storm's propagation speed during the first 20-min integration using the original wind sounding with the experiment employing of R 10 km for each case.

3.2 WRF simulation results

Figure 3 shows the time variation of the maximum vertical velocity from simulated 3D clouds. When a bigger thermal bubble was applied, a convective cloud took longer to develop and reach its maximum vertical velocity for both RICO and IHOP. With the same size of the bubble, RICO, which was moister in the lower atmosphere, took a slightly shorter time to develop than did IHOP. The small peak for each cloud, found before the 4-min integration, was due to the imposed thermal bubble and it weakened as the bubble became larger. It is

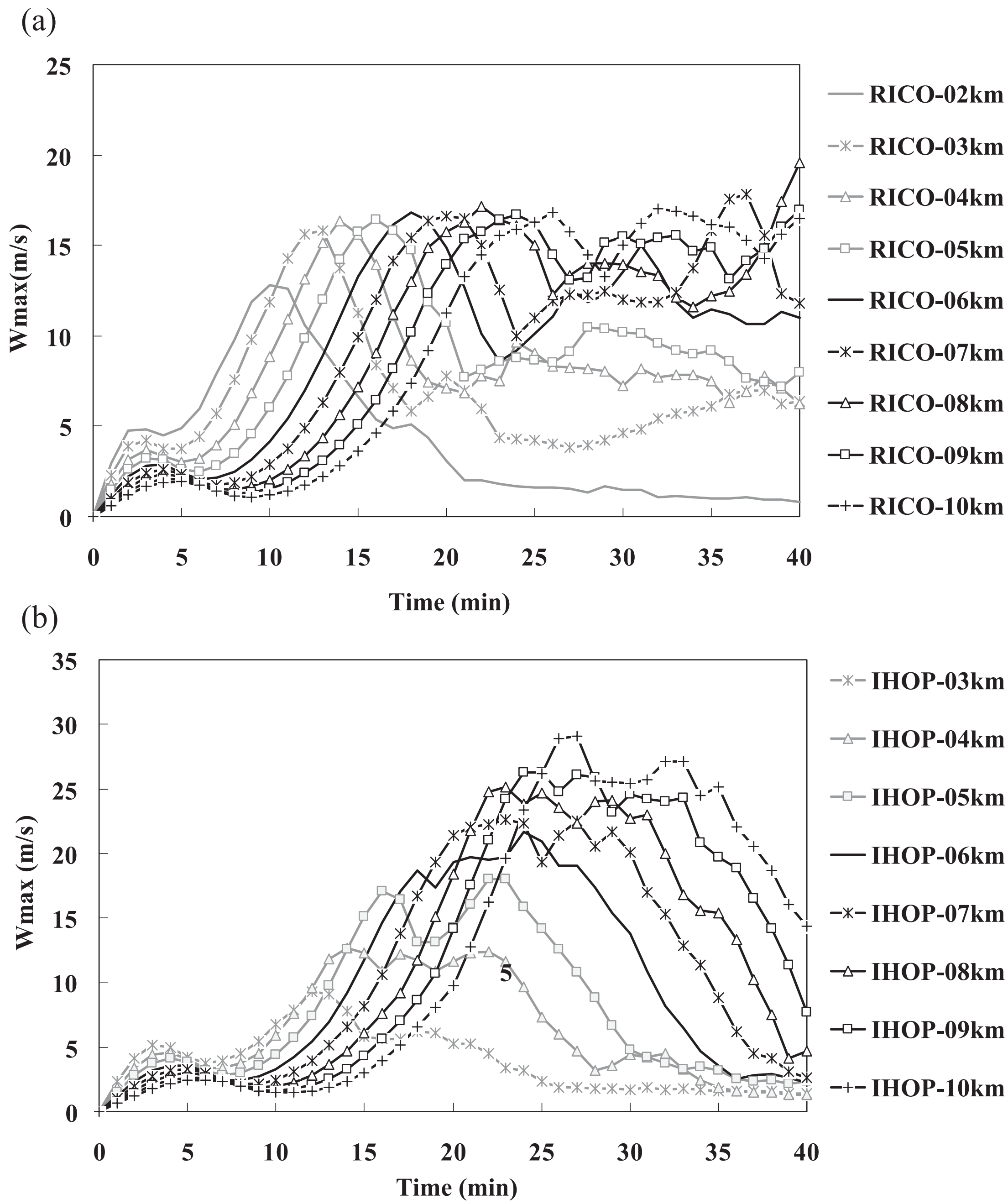

Fig. 3. Time evolution of the WRF simulated maximum vertical velocity with different initial thermal bubble radii for (a) RICO and (b) IHOP.

interesting to see that the peak value of the maximum vertical velocity kept increasing for IHOP (Fig. 3b) but quickly flattened out for RICO (Fig. 3a) as the bubble size increased. The maximum vertical velocity from RICO was stronger than that from IHOP with a small thermal bubble, while that from IHOP was stronger when the radius of the thermal bubble was larger than 5 km. This is probably due to a larger CAPE for the IHOP sounding. Moreover, when a larger thermal bubble was used, the maximum vertical velocity remained at a high value after passing its peak value for RICO, which was due to the development of consecutive multicells. This is similar to the multicell clouds that occur in the middle latitudes. For all IHOP simulations, only one major cloud developed.

The simulated cloud bases were independent of bubble size and were located at approximately the same level (Fig. 4), the lifting condensation level (LCL), in both cases. The cloud base for IHOP was slightly higher than that for RICO because a dryer boundary layer was present in the former sounding (Fig. 2a vs. 2b). In contrast to the cloud base, the simulated cloud top strongly depended on the initial bubble and it reached a greater cloud depth when the bubble size increased. For a given size of the thermal bubble, the cloud top for IHOP was higher than that for RICO when the bubble radius was greater than 5 km. Cloud depth is an essential output of cloud parameterization schemes. The simulated depth is important for the vertical redistribution of dynamic and thermodynamic properties, which is critical to the adjustment of the atmospheric instability. It is important for a 1D cloud model to at least approximately reproduce 3D cloud depth when it is considered in a cumulus parameterization scheme.

It is worth mentioning that the simulated cloud tops were lower than the equilibrium level (EL), where the temperature of the air parcel ascending adiabatically from near the surface is equal to the environmental temperature, particularly for small clouds. The height of the estimated EL was about 13 km for the RICO sounding and about 15 km for the IHOP sounding (Figs. 2a, b). The turbulence diffusion within the cloud and through the lateral boundary has a negative impact on the cloud development. Moreover, the dry air intrusion into a cloud can cause evaporative cooling, which tends to suppress the cloud development. These processes are ignored when a parcel ascends adiabatically. Therefore, the use of the EL as the top of the subgrid-scale vertical adjustment will overestimate the depth of the adjustment.

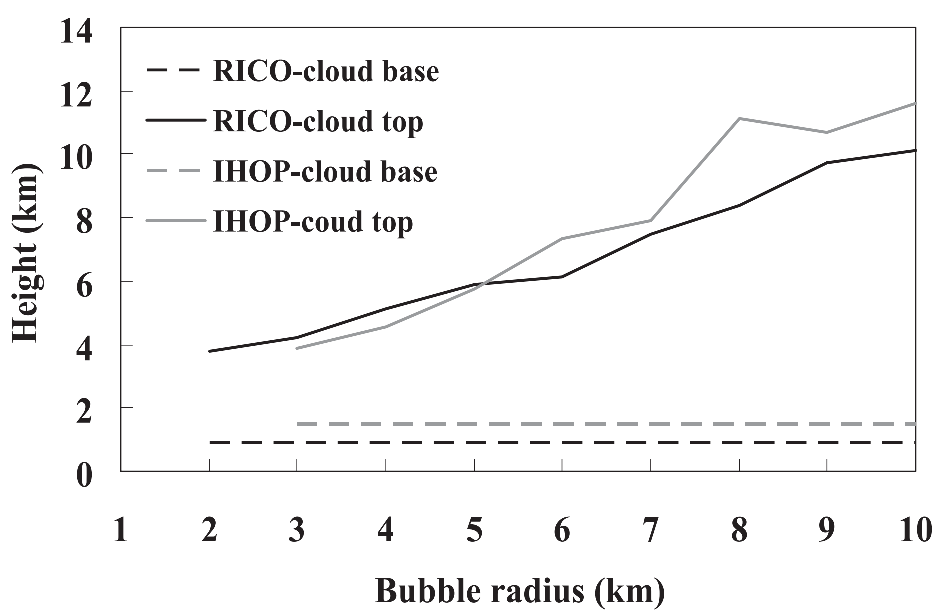

Fig. 4. Height of the WRF simulated maximum cloud top (solid lines) and minimum cloud base (dashed lines) with respect to different thermal bubbles during 1-h model integrations for RICO (black lines) and IHOP (gray lines). The cloud base was defined using the cloud field during the early stage of the cloud development, before precipitation penetrated the cloud base toward the surface.

On the other hand, for any given environment sounding with positive CAPE between the level of free convection (LFC) and the EL, such as the two soundings in this study, clouds with higher tops will consume more of the environment's energy (i.e., CAPE). As a result, in theory, a stronger maximum vertical velocity, which is proportional to the square root of the consumed CAPE, will also occur when the cloud top reaches higher (i.e., larger clouds here). This was shown for the IHOP case but not for RICO (Figs. 3, 4), and the reason behind the behavior of the RICO case deserves further study.

Figures 5a, b show the horizontal cross sections of the vertical velocity at three different levels with a bubble radius of 10 km after a 23-min integration, at the time when the downward motion developed due to detrainment, for RICO and IHOP,

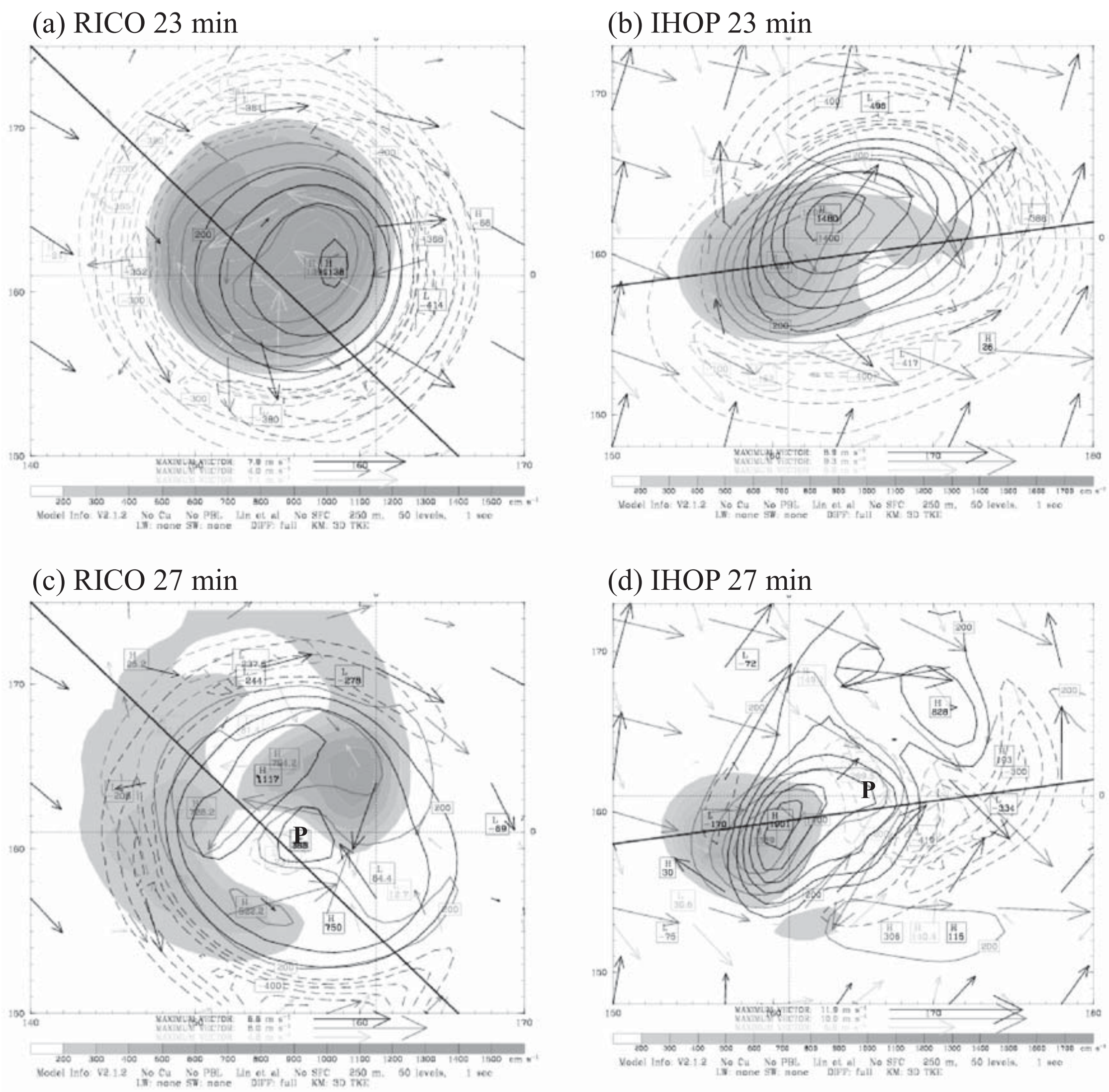

Fig. 5. The horizontal cross sections of vertical velocity (cm s^{-1}) and wind vectors at 1.8 km (shading), 2.7 km (gray lines), and 3.5 km (black lines) after (a) 23 min and (c) 27 min WRF simulations for RICO for the experiment with a bubble radius of 10 km; (b) and (d) are the same information as (a) and (c), respectively, for IHOP at 1.8 km (shading), 3.0 km (gray lines), and 4.2 km (black lines). For each case, negative values at the first plotted level (i.e., 1.8 km) were not plotted, while they were plotted as dashed lines at the other two levels (i.e., 2.7 km and 3.5 km for RICO and 3.0 km and 4.2 km for IHOP).

respectively. The simulated 3D cloud from RICO tilted from the west-northwest to the east-southeast, which is close to the vertical shear direction in Fig. 2c. Due to the multi-directional shear in IHOP, the tilting direction of the simulated 3D cloud changed with height and approximately followed the variation of the vertical shear (Fig. 2d). It is well known that multi-directional shear can sometimes dynamically help support a longer life cycle of a convective cloud such as a supercell cloud (Klemp and Wilhelmson 1978). It is expected that ETTM will have difficulties presenting the influence of the multi-directional shear effect on a long-lived supercell storm on subgrid cloud development. "Can the multi-directional shear effect be parameterized in a 1D cloud model?" This is an interesting question that needs to be examined. Figures 5a, b also show that during the early mature stage of cloud life cycles, downward motions occurred outside the cloud edges, which can be seen in the vertical cross sections in Figs. 6a, b as well. The downward motions mainly resulted from the evaporative/sublimation cooling after the detrainment and advection effects acted on those hydrometeors (letter D in Figs. 6a, b). For IHOP, the locations of downward motions with respect to the cloud at different

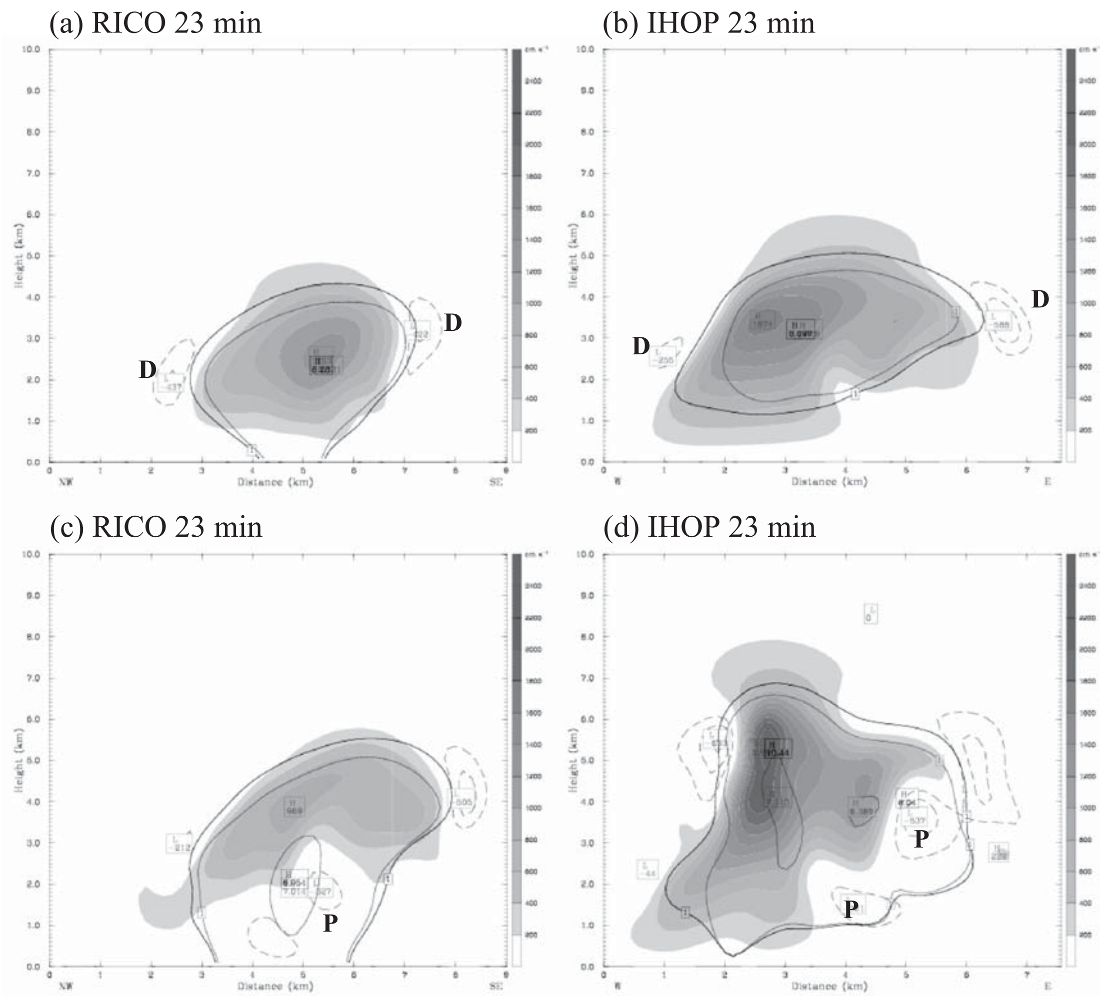

Fig. 6. The vertical cross sections of vertical velocity (cm s^{-1}) for (a) RICO at 23 min, (b) IHOP at 23 min, (c) RICO at 27 min, and (d) IHOP at 27 min for WRF simulations with an initial bubble radius of 10 km. The locations of vertical cross sections in (a)–(d) are indicated in Figs. 5a–d, respectively. The solid black line is the contour line of 1 g kg^{-1} for the total hydrometeors (i.e., cloud edge). The gray lines are the total precipitation (i.e., rain, snow, and graupel) with an interval of 1 g kg^{-1}.

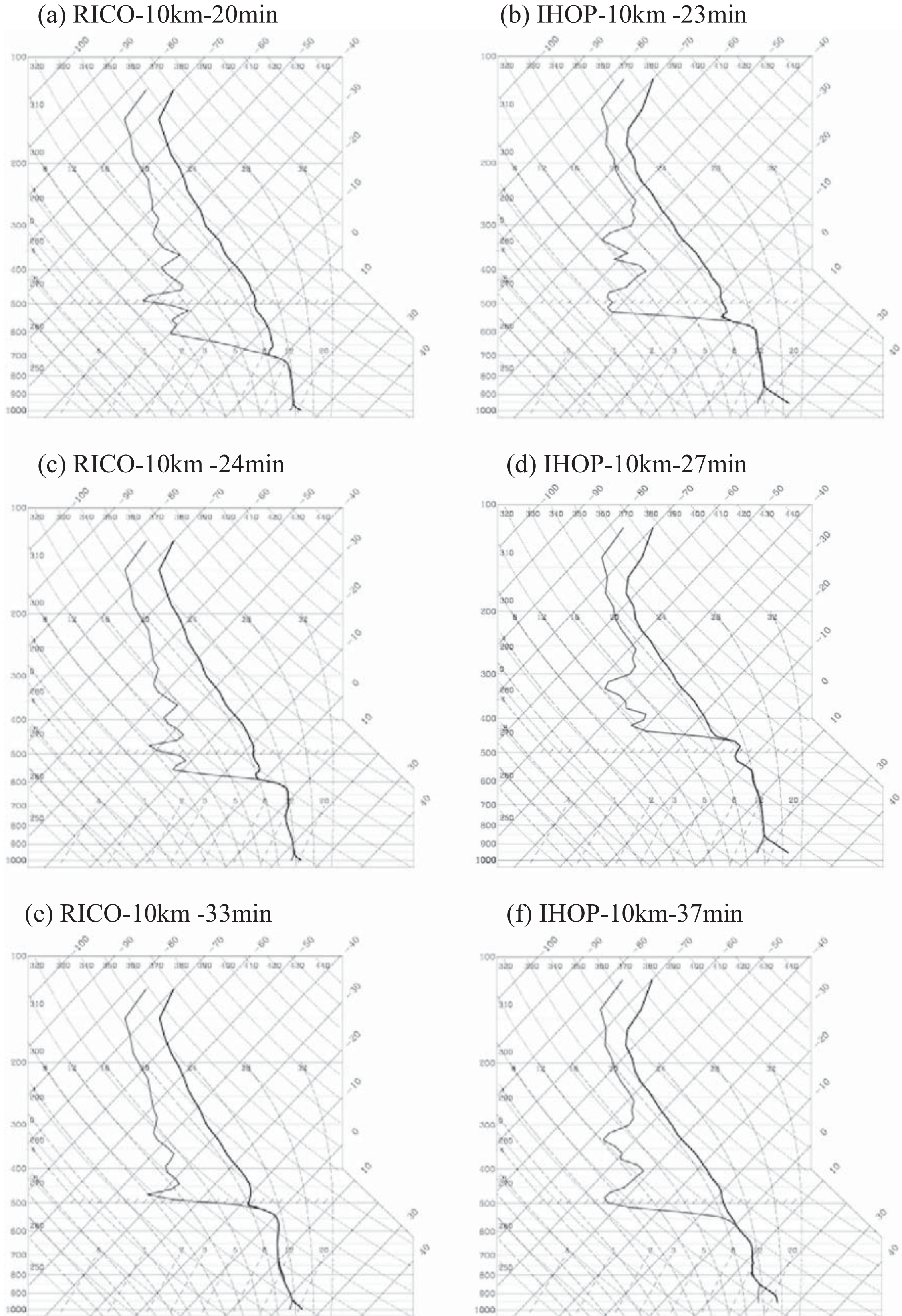

(a) RICO-10km-20min
(b) IHOP-10km -23min
(c) RICO-10km -24min
(d) IHOP-10km-27min
(e) RICO-10km -33min
(f) IHOP-10km-37min

levels reflected the change in the wind direction with height. Four minutes later (i.e., after a 27-min integration), the downward motions developed within and underneath the clouds, located toward the tilting side of the updrafts, and became more evident for both cases (letter P in Figs. 5c, d and 6c, d). These downdrafts were triggered by precipitation that separated from upper-level updrafts, as they were found below the region with the maximum upward vertical velocity (i.e., below the detrainment layers). After the downward motion was initiated, the drag force of precipitation and the cooling effect from the melting of snow and graupel enhanced the downdrafts, in particular for IHOP in the middle latitudes (Tao et al. 1995). With a larger CAPE and a stronger maximum vertical velocity in IHOP for R 10 km, the overshooting above the cloud top was more pronounced (i.e., the top of the updraft was higher than that of the cloud field).

Figure 7 shows the vertical soundings passing the maximum vertical velocity of the convective clouds at different times for the cases with a 10-km bubble radius. During the earlier stages of cloud development, the storm presented a moist adiabatic thermodynamic structure after the convective adjustment occurred for both cases (Figs. 7a, b). A few minutes later, the intrusion of the surrounding dry air into the cloud, which was induced by dynamical mechanisms, resulted in evaporative cooling and caused the inner cloud to deviate from moist adiabatic structures (i.e., 700 hPa to 850 hPa for RICO in Fig. 7c and 480 hPa to 550 hPa for IHOP in Fig. 7d). In the later stage of the cloud life cycle, further mixing with the environment and the breaking of the cloud structure destroyed the moist adiabatic properties of the clouds (Figs. 7e, f), which became unsaturated later during the dissipation stage (figure not shown) when downward motion became dominant. The intrusion of dry air into a cloud can suppress the development of the cloud. It is also expected that ETTM will have difficulties representing this effect. However, the entrainment of the dry air from upper levels of clouds during the dissipation stage is included in ETTM (the latter is through the mass continuity equation).

Usually, the cloud radius and the tilting angle vary with time and height. Since 1D ETTM simulations need inputs for the tilting angle and cloud radius, their approximations from 3D clouds were roughly estimated in this study. At each level, an equivalent cloud radius (R_e) was defined assuming that πR_e^2 was equal to the sum of updraft areas where the upward motion was greater than 2 m s^{-1}. The estimated equivalent cloud radius was a function of height and time. Overall, the maximum equivalent cloud radius increased when the initial thermal bubble size increased (Fig. 8a), where the maximum equivalent cloud radius is defined as the maximum value of the equivalent cloud radius during the time after the cloud develops until it reaches its maximum vertical velocity. It is worth noting that the maximum equivalent cloud radius was smaller than the radius of the initial thermal bubble, particularly for larger clouds. With the same initial perturbation (i.e., the same size of the thermal bubble), the maximum equivalent cloud radius from RICO was comparable or slightly bigger than that from IHOP. Figure 9 shows the time evolution of the vertical profiles of the equivalent cloud radius for the bubble radii of 5 and 10 km from the initial time to the time when the maximum equivalent cloud radius was reached. Results are not plotted for times following the achievement of the maximum equivalent cloud radius because of the development of downward motion, which may lead to an underestimation of the equivalent cloud radius. A small updraft developed before the primary one in Figs. 9a, 9c, and 9d; this was because of the imposed thermal bubble. Note that no such small updraft occurred in the 10-km radius bubble experiment from RICO (i.e., Fig. 9b) as the upward motion due to the thermal bubble did not reach the minimum requirement of 2 m s^{-1} (see Fig. 3a). The maximum equivalent cloud radius was located at the middle to upper levels of the cloud and was shifted upward as the cloud developed. This differs from the assumption of a constant cloud radius made in ETTM. Further study is needed to determine the importance of variations in the 1D cloud model radius.

Instead of estimating the variation in the tilting angle of the cloud with respect to time and height, an averaged angle from the updraft was estimated at the time when the maximum vertical velocity

Fig. 7. The vertical sounding within the 3D cloud passing the maximum vertical velocity after (a) 20-min (c) 24-min, and (e) 33-min simulations for RICO with an initial bubble radius of 10 km; (b), (d), and (f) present the same information but for IHOP after 23-min, 27-min, and 37-min, respectively.

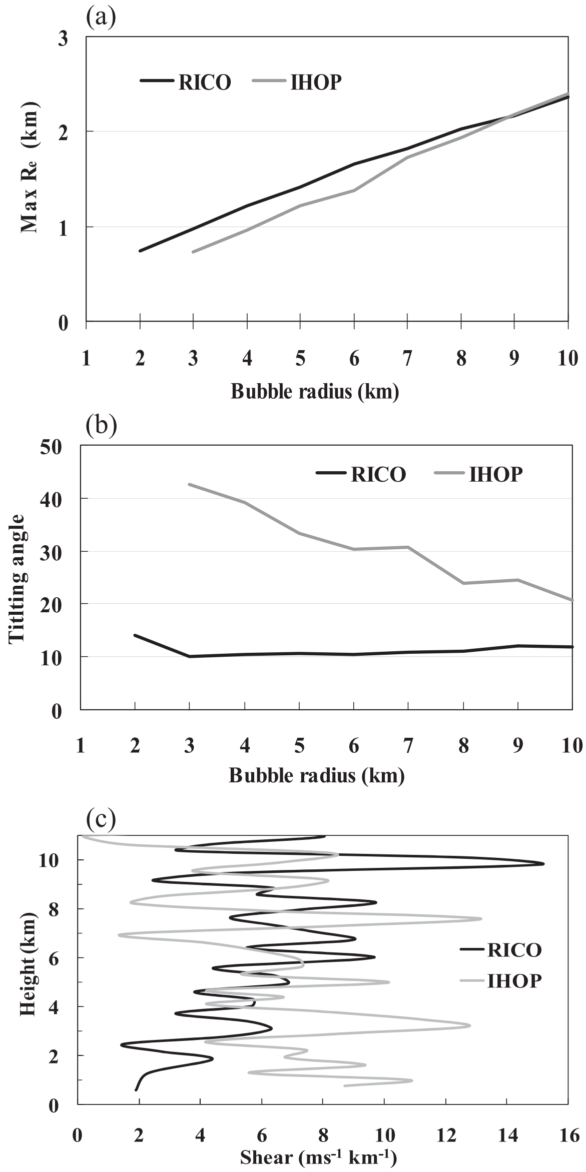

Fig. 8. Estimated (a) maximum equivalent cloud radius (R; km) and (b) tilting angle (°) for RICO (black lines) and IHOP (gray lines) from WRF simulations at the time of occurrence of the maximum vertical velocity; (c) the smoothed vertical shear from model initial conditions for both cases.

was reached and this was used for ETTM simulations. To estimate the angle, the equivalent centers at two selected levels within the updraft were first identified. The upper level was at about 1/4 of the cloud depth from the cloud top, and the lower level was at about the same depth from the cloud base. The equivalent center point, (x, y) at each level, was the average of the locations for grid points with vertical velocity greater than 2 m s^{-1}, which is similar to the criteria used for the equivalent cloud radius. The ratio of the horizontal displacement (ds) to the vertical displacement (dz) between these two points was used to estimate the cloud tilting angle (α_o) using the formula, $\alpha_o = \tan^{-1}(ds/dz)$.

Figure 8b shows that the tilting angle was almost constant (about 10°) with respect to different bubble sizes for the RICO case. However, for the IHOP case, the averaged tilting angle decreased when the bubble size increased and values ranged from about 20° to 40°. In general, one expects that a cloud will tilt to a greater extent when the environment shear is stronger. Figure 8c shows the vertical shear profiles that were estimated from the initial soundings for both cases. The figure has been smoothed by taking the average of every 3, 5, 7 9, and then 11 grid points (i.e., smoothed a total of five times by averaging over different numbers of grids each time) since the original soundings were very noisy. Note that only the values below 11 km, the maximum cloud height in this study, are plotted. Although the shear was highly variable in the vertical direction, the averaged shear for IHOP in the plotted domain is stronger than that for RICO, as expected since IHOP is a sounding from the middle latitudes. The figure also shows that overall, the shear increased with height for RICO, while it stayed more or less constant with height for IHOP. Therefore, for RICO, a cloud would be affected by a stronger averaged shear environment when the cloud developed deeper (i.e., a larger cloud), which in turn would have made the cloud tilt to a greater extent. On the other hand, under a constant shear profile, a larger cloud can potentially tilt to a lesser extent because of its larger inertial effect. The combination of these two effects, i.e., shear and the size of the cloud, caused the simulated tilting angle to stay close to a constant with respect to different cloud sizes for RICO, while the angle decreased when a cloud became larger for IHOP.

4. ETTM simulation results and comparison with WRF simulations

4.1 Experiment design

The same initial soundings as in the WRF simulations (Fig. 2) were used in ETTM, except that horizontal winds were set to zero. The stretched res-

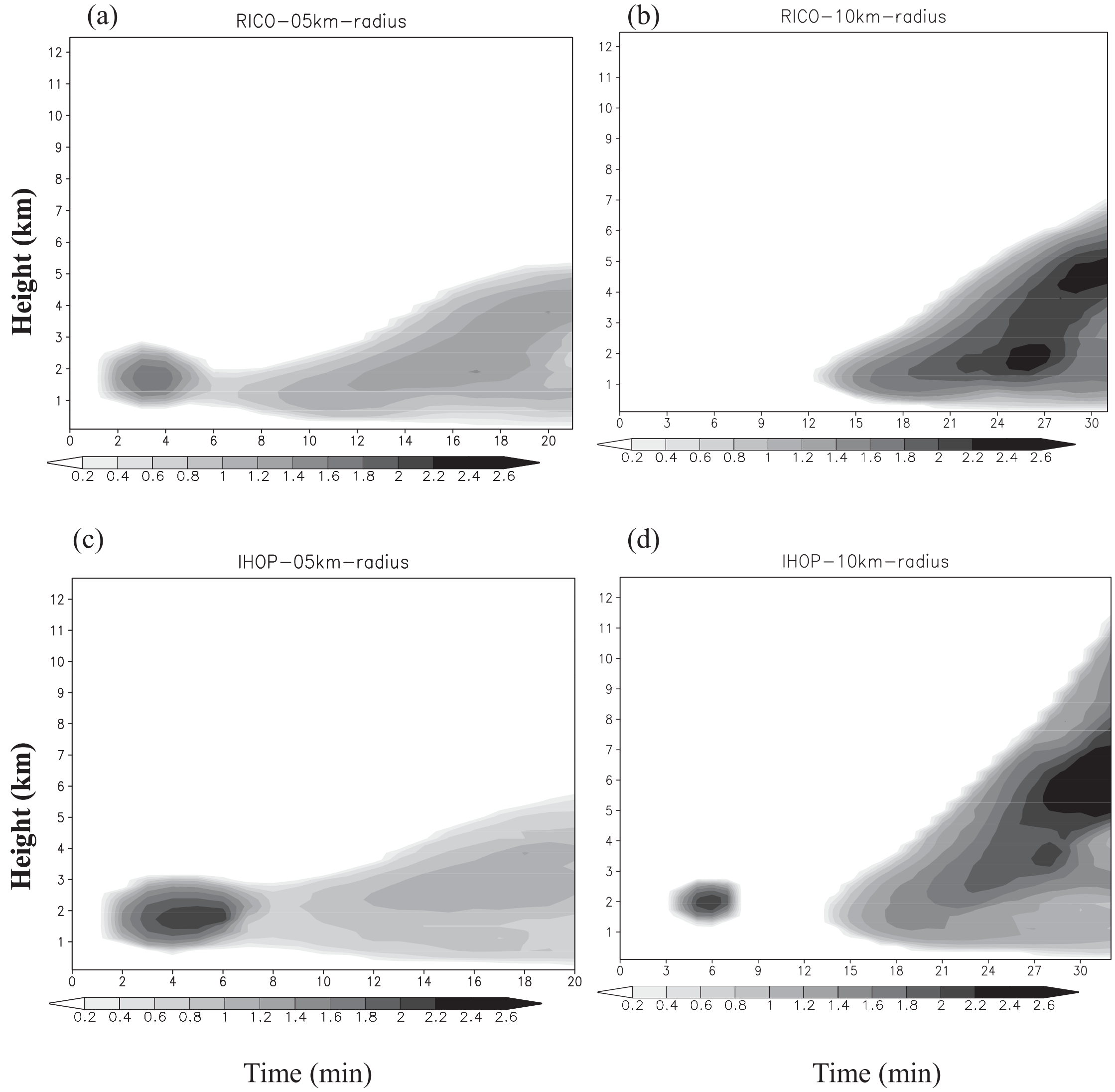

Fig. 9. Time evolution of the vertical profiles of the equivalent cloud radius (km) from initial time to the approximate time when the maximum equivalent cloud radius was reached for the WRF experiments with bubble radii of (a) 5 km and (b) 10 km from RICO; (c) and (d) are the same as (a) and (b), respectively, except from IHOP.

olution and grid size in the vertical were the same as those in WRF simulations. ETTM experiments with various cloud radii and tilting angles were conducted to mirror each WRF simulation (i.e., nine bubble size experiments for RICO and eight for IHOP). For convenience, ETTM experiments were named following the convention Exxkm, where E indicates the ETTM model and "xx" indicates the radius of the thermal bubble in the WRF simulation. As mentioned earlier, the tilting angle and the cloud radius in ETTM were assumed constant during the model integration, and they were specified at the initial stage. Before parameterizing the tilting angle and cloud radius using environment or grid-scale soundings, we assessed how ETTM performs when the best of both parameters are provided. In the ETTM simulations conducted here, both parameters were directly estimated from simulated 3D clouds from WRF, and the estimated maximum equivalent cloud radius and the tilting angle shown in Fig. 8 were used. Results from ETTM were then compared with those from 3D cloud simulations to evaluate ETTM's performance. For each experiment, the thermal bubbles used in ETTM simulations were also estimated from horizontally averaged potential temperature perturbations in WRF simulations (within the area of the estimated 3D updraft).

4.2 *ETTM simulation results and comparison with WRF results*

Figures 10 and 11 show the updrafts and downdrafts from E10km runs for RICO and IHOP, respectively. The simulated updrafts from ETTM (i.e., Figs. 10a, 11a) developed right after the model integration (i.e., no time lag), while it took about 10 to 15 min for a 3D cloud to develop (see Figs. 9b, d). This implies that a time delay might be needed for subgrid cloud development if ETTM is used in a time-dependent cumulus parameterization scheme and that the delay will depend on the size of the convective cloud. Downdrafts quickly developed before updrafts reached their mature stage (Figs. 10b, 11b). For RICO, the maximum downdraft developed at the same levels as that of the upper-half portion of the updraft during the early stage and shifted toward the surface in the dissipation stage. The 1D cloud life cycle was shorter and both the updraft and downdraft were weaker for the IHOP case when compared to those for the RICO case, which shows the opposite features of the 3D cloud results.

The maximum vertical velocity from ETTM and WRF with respect to different maximum equivalent cloud radii R_e (i.e., different sizes of bubbles) are plotted in Fig. 12. For both cases, the maximum vertical velocities from 1D clouds (i.e., ETTM in Fig. 12) were much weaker than those from 3D clouds (WRF-wmax; i.e., the maximum point value during a 3D cloud life cycle), as expected; however, most of them were also weaker than the maximum of the horizontally averaged vertical velocity within the 3D updraft during the cloud life cycle (WRF-avg). The WRF horizontally averaged vertical velocity was calculated as the average of vertical velocities using grid points in which values were greater than 2 m s^{-1} at the same height. For the IHOP case, the maximum averaged value from WRF increased when the maximum equivalent cloud radius (i.e., bubble size) increased, while that from ETTM remained almost constant or slightly decreased when the cloud radius increased.

The simulated cloud tops and bases from ETTM were also examined since they are important to the vertical adjustment of the mass, momentum, heat, and moisture variables in cumulus parameterization. Note that no cloud developed for the E02km run from IHOP, and therefore, no results are plotted for this experiment. The simulated 3D cloud bases, which were close to the lifting condensation levels, were well reproduced by ETTM with different equivalent cloud radii for both RICO and IHOP (Fig. 13). However, the 1D cloud tops were significantly underestimated; in particular, those from IHOP were capped at about a 3–4 km height. Moreover, the cloud life cycle became shorter for IHOP ETTM simulations when the cloud radius became bigger, which is the opposite of its counterpart from the 3D cloud (figure not shown), indicating that ETTM results got worse when the cloud radius increased for the IHOP case. Overall, the simulated 1D cloud results for IHOP were worse than those for RICO. The underestimation of the cloud strength from ETTM was expected since the 1D cloud presents the average of a 3D cloud, and therefore, the penetration effect of the 3D updraft core was under-represented. Moreover, some mechanisms in a 3D cloud, such as the multi-directional shear effect, cannot be explicitly included, and some simplifications were made in the 1D cloud representation. The possibility for the improvement of these simplified, simulated 1D clouds are examined by conducting some sensitivity tests in the next section.

4.3 *ETTM sensitivity tests*

a. *Moisture*

During the time taken for a 3D cloud to develop with a thermal bubble (Fig. 3), the atmospheric boundary layer in the updraft region was moistened due to low-level convergence before the cloud developed. This is consistent with the difference in time delay for 3D cloud development between RICO and IHOP. A shorter lag time was required for RICO since its lower atmosphere was more moist. In ETTM, the convergence/divergence effect was taken into account (i.e., through the continuity equation). However, the 1D cloud developed right after the model integration (Figs. 10, 11). Therefore, no moistening in the lower atmosphere occurred before the 1D cloud developed. To account for this process, for each ETTM simulation, two sensitivity runs with different moistening assumptions within the thermal bubble of the updraft were conducted (i.e., use of a moistened thermal bubble). The Relative Humidity (RH) within the thermal bubble was specified as follows:

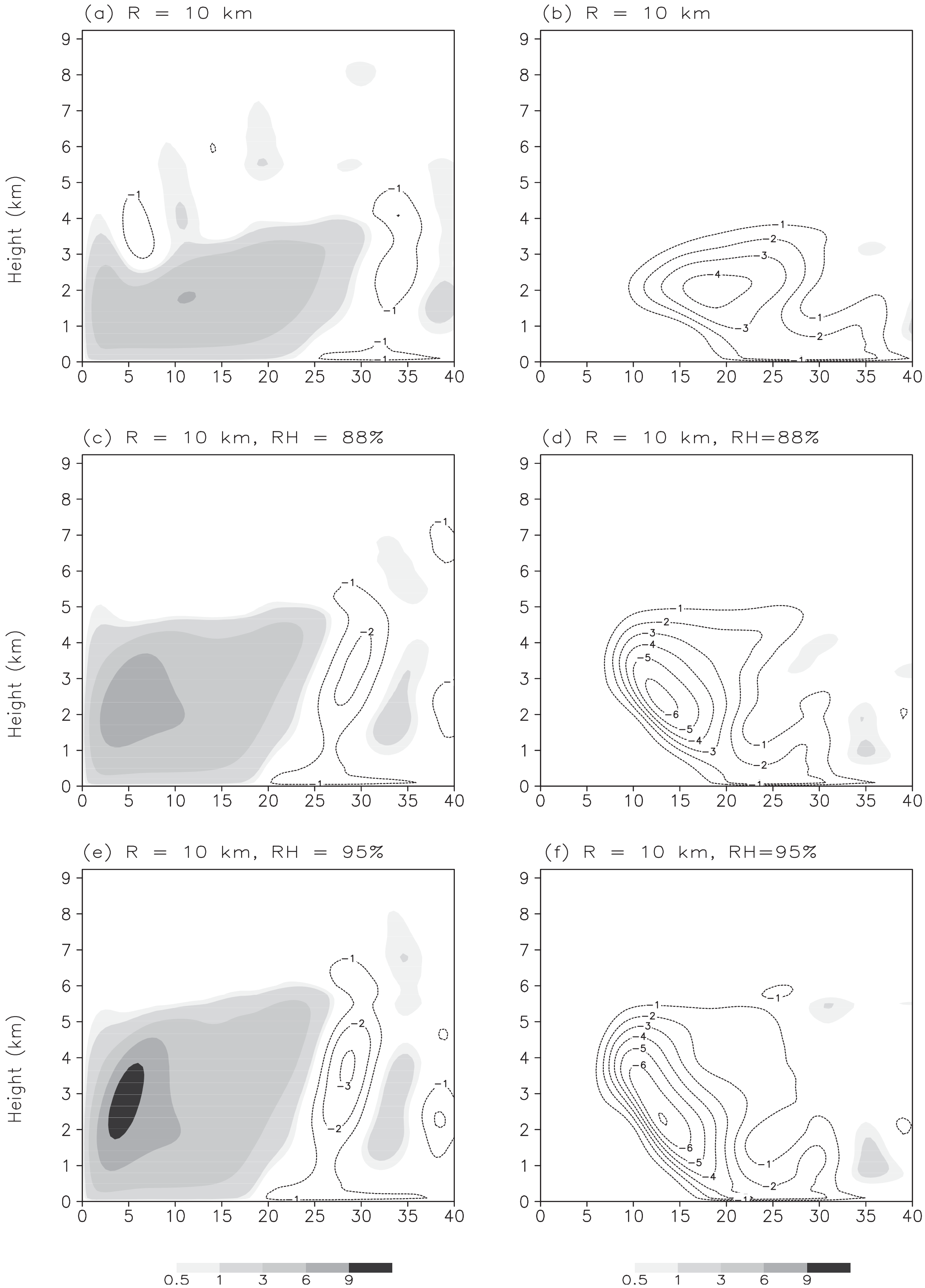

Fig. 10. Time evolution of vertical velocity (m s^{-1}) from the (a) updraft and (b) downdraft from E10km for the RICO case; (c) and (d) are the same as (a) and (b), respectively, except from the ER88 experiment and (e) and (f) from the ER95 experiment.

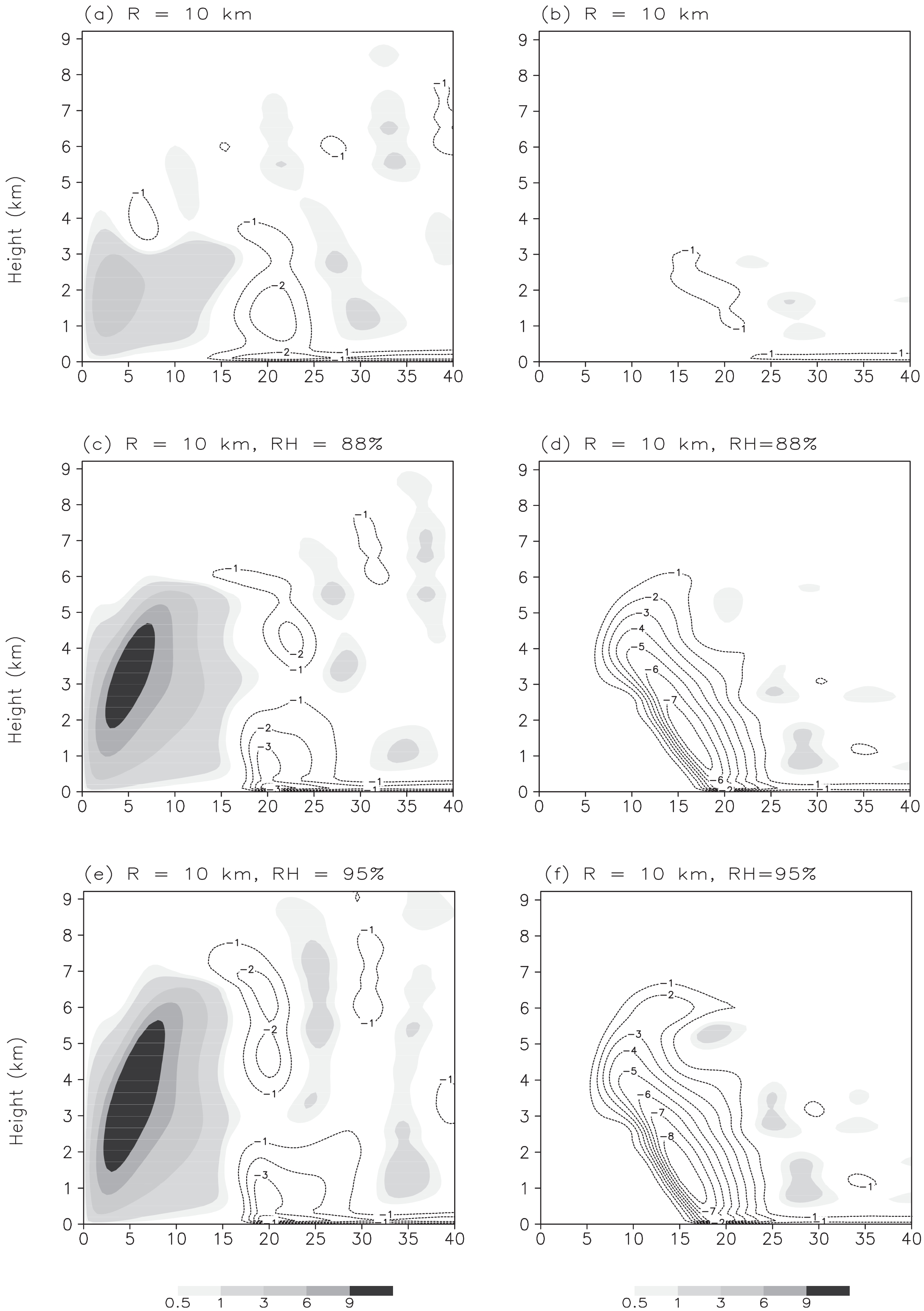

Fig. 11. Figure legends are the same as those in Fig. 10, except for the IHOP case.

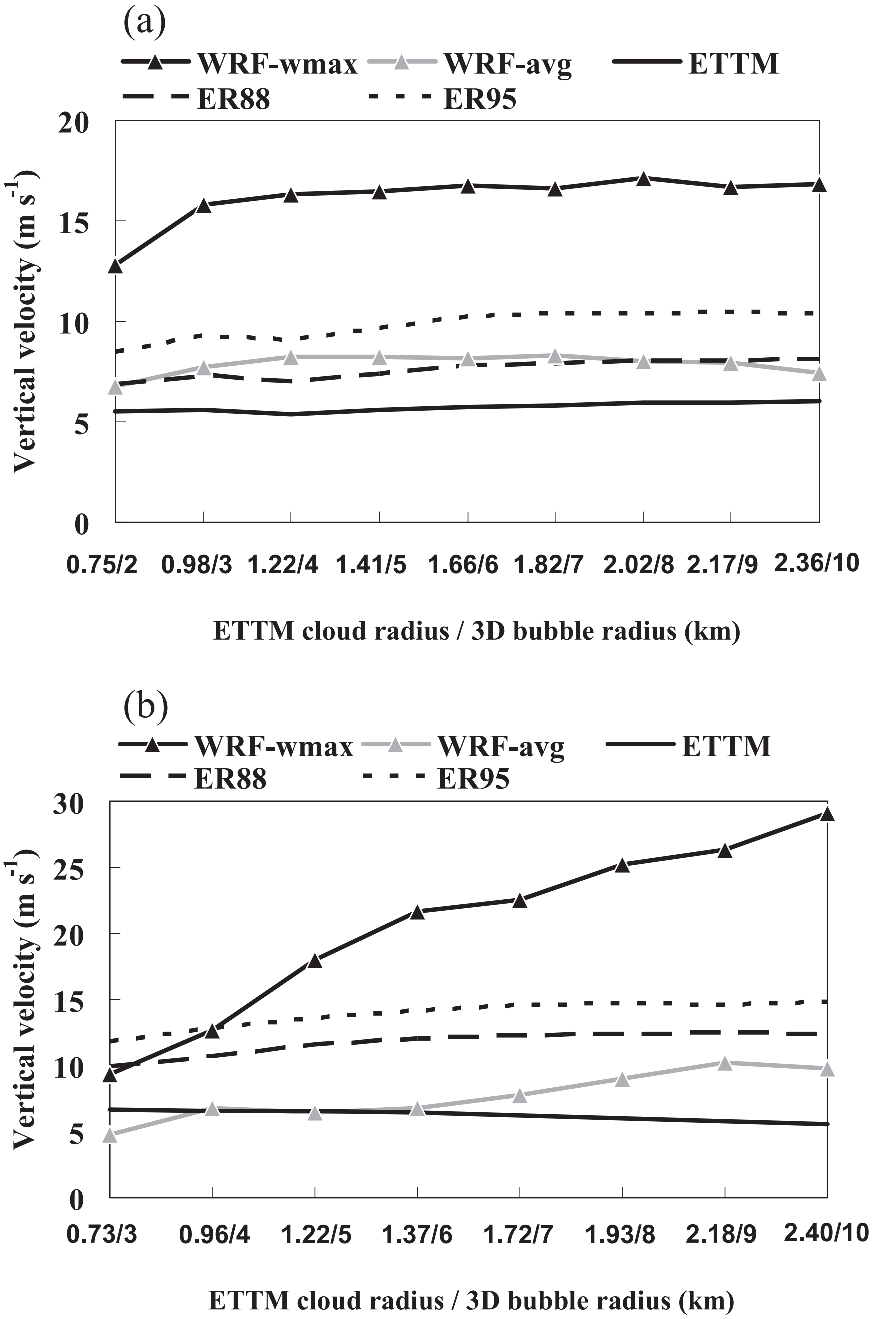

Fig. 12. The WRF-simulated maximum vertical velocity (WRF-wmax), the WRF maximum horizontally averaged vertical velocity, and the ETTM maximum vertical velocity with the original thermal bubble (ETTM) and with different relative humidities within the thermal bubble (i.e., ER88 for the 88% humidity run and ER95 for the 95% humidity run) with respect to different ETTM cloud radii (or 3D bubble radii) for (a) RICO and (b) IHOP.

$$RH = \begin{cases} \max(RH_o, RH_c), & z < 3 \text{ km} \\ RH_o, & z \geq 3 \text{ km} \end{cases},$$

where RH_o is the original RH in the initial sounding, and RH_c is the lower bound of the relative humidity within the bubble. Two different RH_c

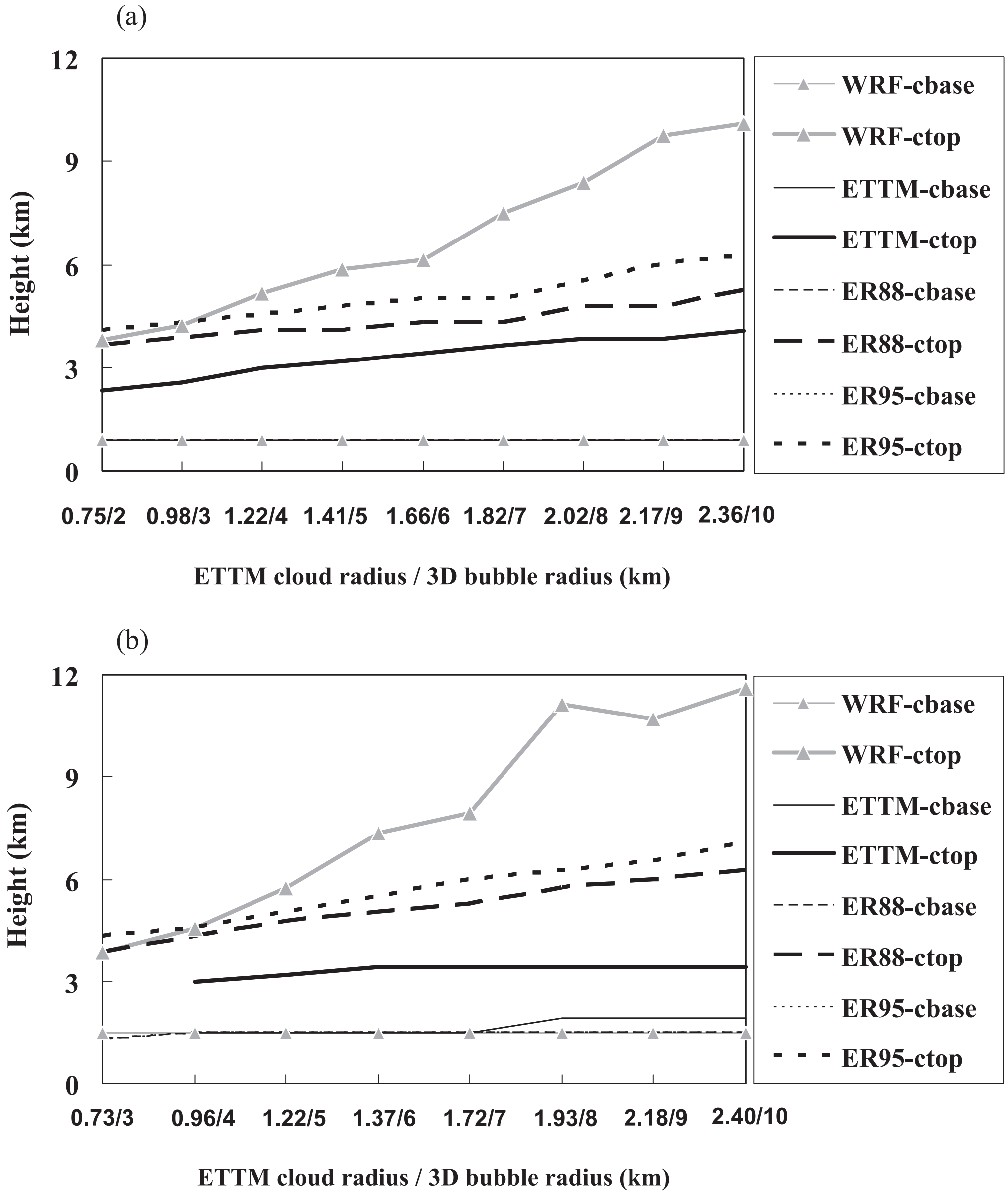

Fig. 13. The simulated cloud top and base with respect to different cloud radii (or 3D bubble radii) from WRF and ETTM with sensitivity tests of different low-level relative humidities from (a) RICO and (b) IHOP. Note that the base lines overlap from different runs and are therefore not apparent. No cloud developed in the ETTM simulation for the cloud radius of 0.73 km with the original thermal bubble for the IHOP sounding.

values, 88% and 95%, were examined and sensitivity trials were named ER88 and ER95, respectively. The value of 88% was chosen since it was the value used by Schlesinger (1978) and Chen and Sun (2002, 2004).

With a fixed cloud radius, the intensity of the simulated 1D cloud was clearly improved when the low-level moisture was increased. The cloud developed deeper and the maximum vertical velocities became stronger for both updraft and downdraft (Figs. 10–13). In particular, for IHOP, increased moisture allowed clouds in larger bubble simulations to penetrate the cap at a 3–4 km height that occurred in the original bubble simulations discussed in Section 4.1. More moisture was able to further enhance simulated 1D cloud intensity (i.e., ER88 vs. ER95) for both cases. Different values of relative humidity (RH_c) might be needed for different sizes of 1D cloud simulations, and this requires further study. The maximum vertical velocity from ER88 was close to the maximum average value from WRF for RICO. For IHOP, with either ER88 or ER95, the maximum vertical velocity was stronger than the maximum averaged value from WRF simulations and again, remained close to constant; however, it increased slightly when the cloud radius increased (Fig. 12). Although the simulated cloud depths were improved in both cases, they were still underestimated when compared with 3D clouds (Fig. 13).

Horizontally integrated vertical mass (F_m), heat (F_h), and moisture (F_q) fluxes from 3D WRF (i.e., horizontal integration) and 1D ER95 (i.e., summation of updraft and downdraft) simulations were calculated using the following formulae:

$$F_m = \int \rho w \, dA, \tag{1}$$

$$F_m = \int C_p \rho w (\theta - \theta_o) \, dA, \tag{2}$$

$$F_m = \int \rho w (q - q_o) \, dA, \tag{3}$$

where ρ is the density; w, the vertical velocity; C_p the specific heat of air at constant pressure; q, the mixing ratio; and A, the horizontal coverage area of the cloud. The subscript 0 indicates the initial conditions. Time variation results for the bubble radii of 5 km and 10 km for RICO (Fig. 14) and IHOP (Fig. 15), respectively, are presented. A minimum magnitude of 2 m s^{-1} of the vertical velocity (i.e., both upward and downward motion) was required for the calculation of the fluxes since only updrafts and downdrafts were considered. Since the simulated cloud depth is important to the vertical adjustment of variables and that from ER95 reproduced the 3D cloud depth better than those from ER88 and the original bubble simulations, only results from ER95 are presented.

The depth of the vertical distribution of fluxes was shallower from ER95, as expected, since the 1D cloud top did not reach as high as that of the 3D cloud. For the RICO case, ETTM erroneously produced negative mass flux near the surface, which was caused by the downdraft at the dissipation stage. For IHOP, the negative flux in ER95 was located at a very low altitude, and this was also caused by the downdraft. The elimination of the problem of negative flux will require improvements in the ETTM downdraft. Moreover, the WRF vertical fluxes for IHOP were sustained over a longer time than those from the 1D cloud because the 1D cloud life cycle was very short.

Although there were discrepancies between WRF and ER95 simulations, the flux patterns from both models showed some similarities such as in shape. For RICO, WRF produced negative mass flux (Fig. 14a) at the upper half cloud height and this was reproduced by ER95 (Fig. 14b); moreover, the negative heat fluxes due to overshoot cooling above the cloud top and at the middle- to upper-level height of the cloud during the later stage of the cloud life cycle were presented by both models. These positive results show that ETTM has the potential for use in cumulus parameterization, given further improvements in performance, in particular, for downdraft and cloud depth.

It was noticed that the magnitudes of fluxes from the 1D cloud were larger than those from the 3D cloud after adding moisture into the thermal bubble (Figs. 14, 15). This might be due to a larger maximum vertical velocity when compared with the maximum averaged value from the 3D cloud (Fig. 12), and it may be overcome using a partial cloud approach (i.e., less than one full cloud effect) in cumulus parameterization.

b. Tilting angle and the downdraft radius

Using the ER95 configuration, sensitivity tests with a zero-degree cloud tilting angle (named ER95A0) or with the ratio of the downdraft radius to the updraft radius equal to 1 (named ER95R1) were conducted. Only RICO with a bubble size of 5 km and IHOP with a bubble size of 10 km are presented.

The differences of simulated mass, heat, and moisture fluxes of ER95A0 from ER95 are shown in Fig. 16. The patterns of the differences from RICO and IHOP with bubble sizes of 5 km and 10 km, respectively, are quite similar. However, the values are larger and the patterns are deeper for IHOP due to the use of a larger thermal bubble. When compared with ER95, the erect cloud in ER95A0 produced more upward mass flux (Figs. 16a, b), indicating that the inclusion of downdraft can reduce the upward mass flux. The total reduction for the time-integrated mass flux during the

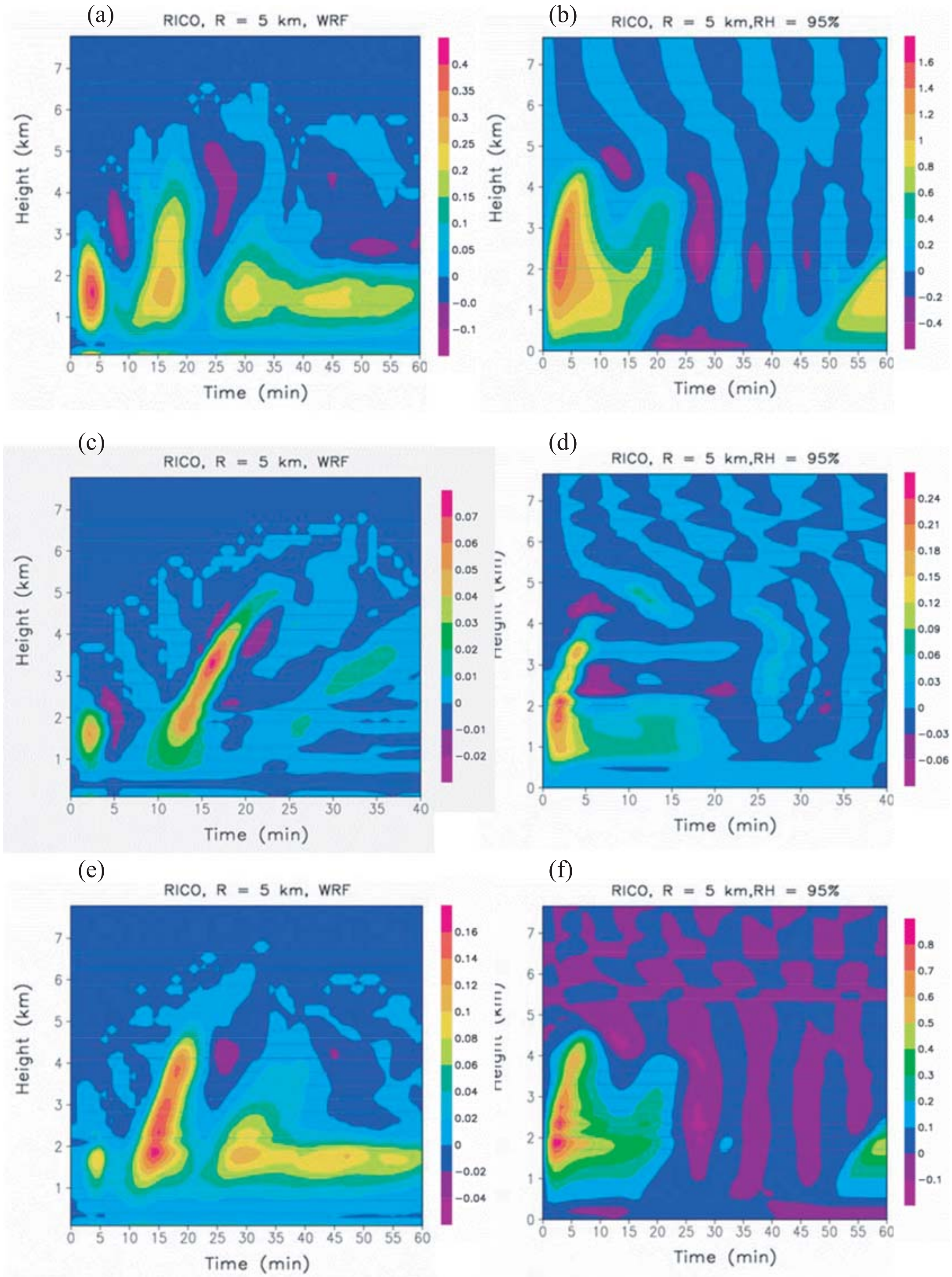

Fig. 14. The simulated (a) mass ($\times 10^8$ kg s^{-1}), (c) heat ($\times 10^{12}$ J s^{-1}), and (e) moisture ($\times 10^6$ kg s^{-1}) fluxes from WRF simulations for the RICO case when the bubble size is 5 km; (b), (d), and (f) are the same as (a), (c), (e), respectively, except from the corresponding 1D cloud simulation from ER95.

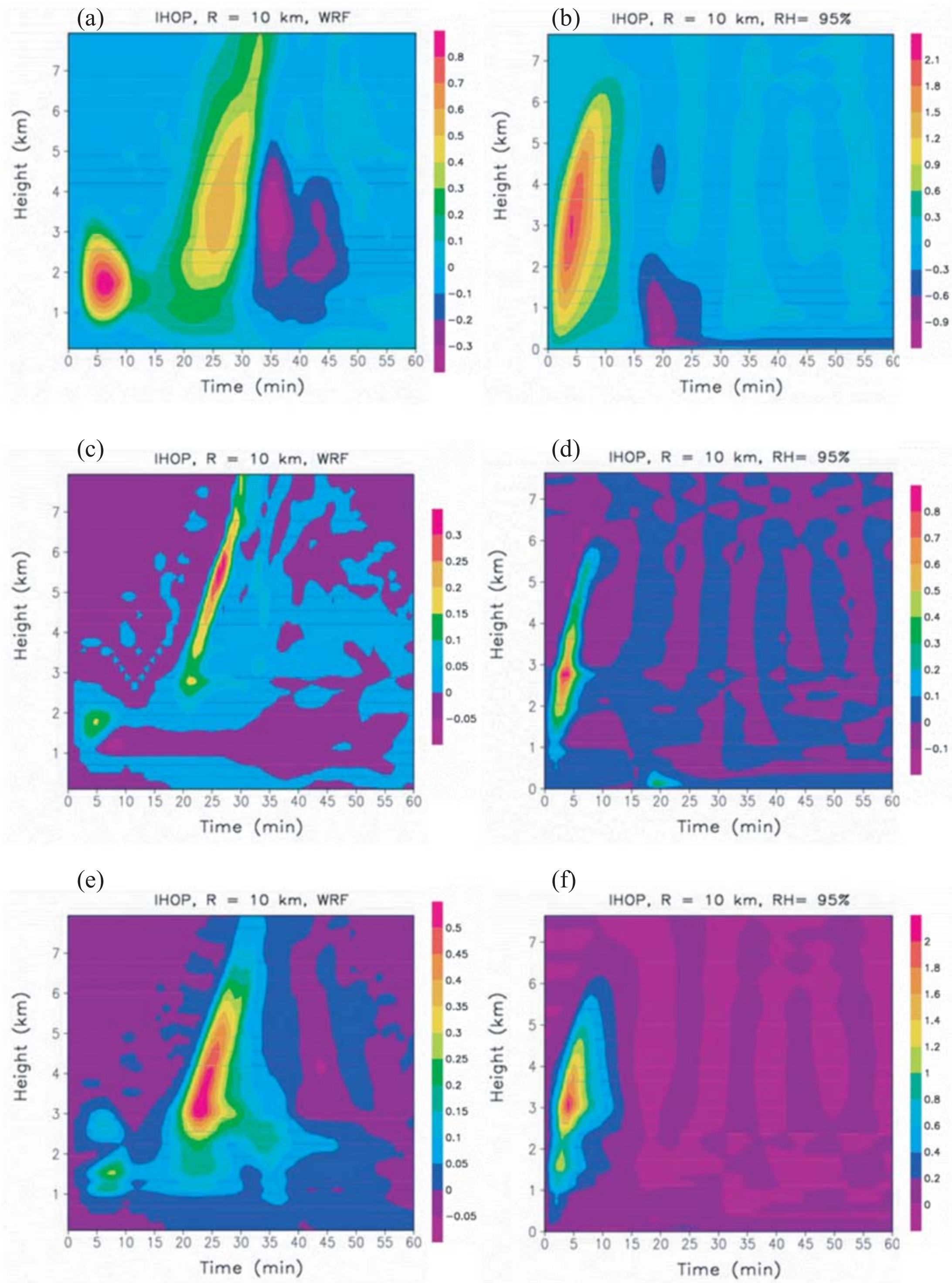

Fig. 15. Figure legends are the same as those in Fig. 14, except for the IHOP ER95 run with the bubble size of 10 km.

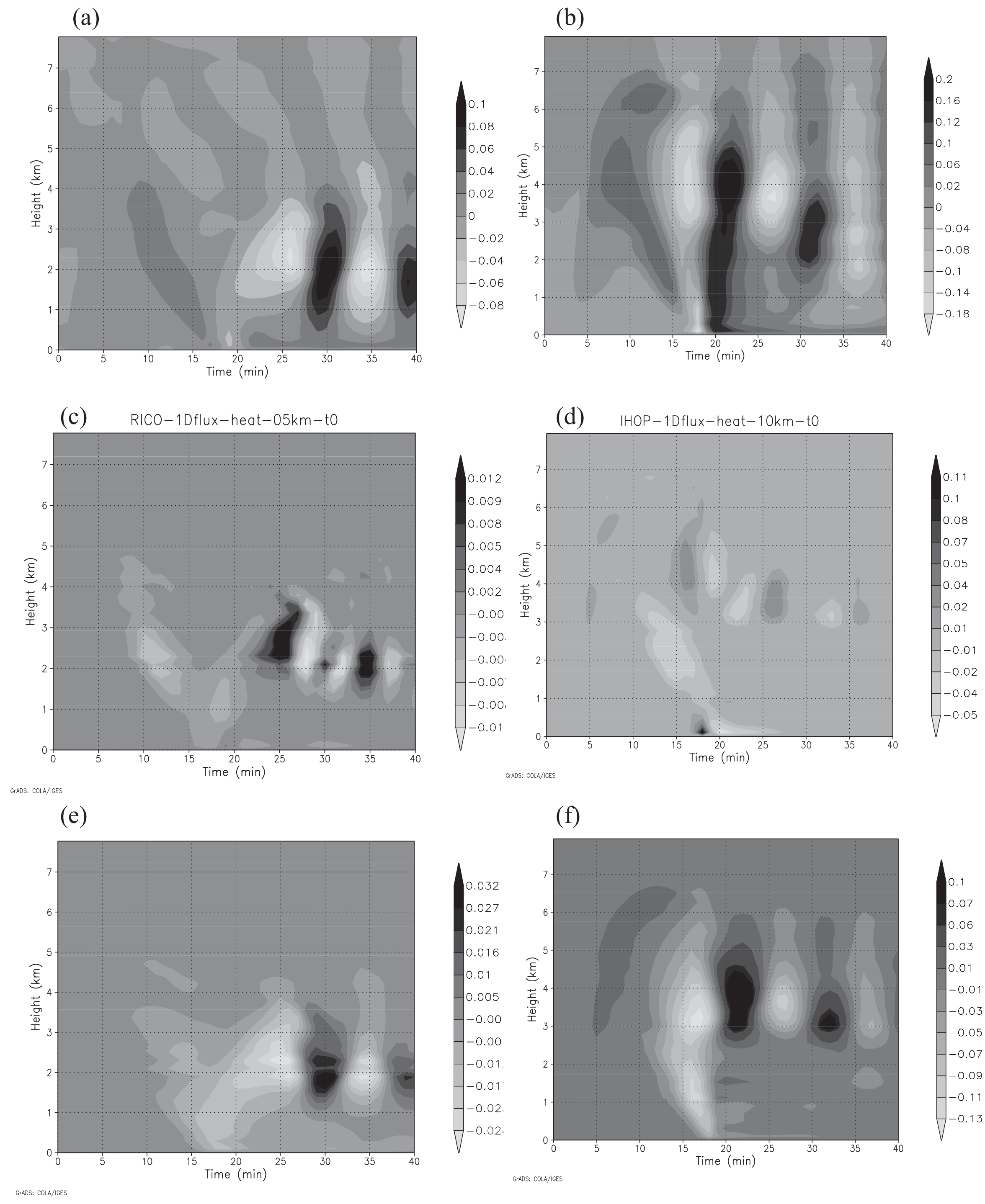

Fig. 16. The differences of simulated (a) mass ($\times 10^8$ kg s^{-1}), (c) heat ($\times 10^{12}$ J s^{-1}), and (e) moisture ($\times 10^6$ kg s^{-1}) fluxes between ER95A0 and ER95 (i.e., ER95A0–ER95) for the RICO case with the 5-km bubble size; (b), (d), and (f) are the same as (a), (c), (e), respectively, except for the IHOP case with the 10-km bubble size. Note that different color scales are used in different figures.

cloud life cycle reached up to 20% at some levels for IHOP (figure not shown). On the other hand, the erect cloud leads to an underestimation of the upward heat and moisture fluxes (Figs. 16c–f). The underestimation of upward heat and moisture fluxes is a problem for the simulated 1D cloud after the deep convection starts dissipating (Figs. 14, 15), except for the heat flux from RICO ER95, which is overestimated at low levels (Figs. 14c, d). However, it is worth mentioning that the magnitude of the heat flux differences between ER95 and ER95A0 for RICO is much smaller than that for IHOP (Figs. 16) because of a smaller tilting angle in RICO (Figs. 16c, d). Overall, the downdraft due to the tilting of the cloud is able to slightly improve low-level upward heat and moisture fluxes for these two case studies.

The differences in simulated mass, heat, and moisture fluxes between ER95R1 and ER95 are shown in Fig. 17. The patterns of the differences from RICO and IHOP are also quite similar, except for those in the low atmosphere. The differences are more pronounced with the use of a larger bubble size (i.e., IHOP), similar to the previous sensitivity test. Compared with ER95, in which the downdraft radius was 40% of the updraft radius, the maximum downward motion was weaker in ER95R1 (figures not shown). This is because the same amount of hydrometeors was distributed over a larger horizontal area when a larger downdraft size was applied. In addition, the maximum downward motion was also shifted upward and occurred later in time. When compared with ER95, although the maximum downward motion was weaker in ER95R1, a larger size of the downdraft made the reduction of the total upward mass flux more prominent, except for the lower levels in RICO's ER95R1. However, the weaker downward motion in the downdraft of ER95R1 made the potential temperature anomalies much more unorganized. In turn, the upward heat flux became weaker (i.e., negative differences in Figs. 17c, d), which was unanticipated. Results indicate that when compared with the simulated 3D clouds, the use of a larger downdraft size in ETTM improved the heat flux for IHOP but slightly degraded the heat flux for RICO. For moisture flux differences in Figs. 17e, f, negative values occurred earlier in time and positive values occurred later in time because the maximum downward motion took place at a later time for ER95R1. The difference in the time integrated total moisture flux during the cloud life cycle between ER95R1 and ER95 was much smaller than that between ER95A0 and ER95, except for the lower levels. Upon combining the heat and moisture flux comparisons, the influence of using different downdraft sizes on 1D cloud simulation results is not clear from these two case studies.

5. Concluding remarks

The Weather Research and Forecasting (WRF) model, which was developed in a cloud-resolving mode, and Explicit Time-dependent Tilting Cloud Model (ETTM) were used to simulate three-dimensional (3D) and one-dimensional (1D) cloud properties, respectively, under two different atmospheric environments. One is a sub-tropical maritime sounding from the Rain in Cumulus over the Ocean (RICO) experiment and the other is a mid-latitude continental sounding from the International H_2O Project (IHOP). For the IHOP case, the convective available potential energy (CAPE) was higher (2450 J kg^{-1} for IHOP and 1400 J kg^{-1} for RICO) and the lower atmosphere was drier when compared with the corresponding values for RICO. The vertical wind shear direction varied with height for IHOP, while it was almost uniformly directed for RICO.

The ETTM consists of an updraft and a downdraft and was developed for potential use in cumulus parameterization (Chen and Sun 2004). The updraft was initiated by a thermal bubble, while the downdraft was triggered by the drag force and evaporative/sublimation/melting cooling of detrained hydrometeors and departed precipitation from the updraft (Fig. 1). Both WRF and ETTM are non-hydrostatic models and the same microphysics scheme was used in both models for this study.

For both RICO and IHOP, 3D cloud simulations were conducted under a horizontally uniform realized condition and initialized with different radii of thermal bubbles. There was a time lag between the model initial time and the 3D cloud development time, and the delay increased as the bubble radius increased. Moreover, the delay can be longer if the lower atmosphere is originally drier (i.e., the IHOP case). The tilting direction of the 3D cloud strongly correlated to its environmental shear, and the tilting angle from RICO was smaller than that from IHOP, which is consistent with observed clouds in the tropics versus the mid-latitudes. For RICO, WRF simulations produced multi-cells, i.e., the successive formation of convec-

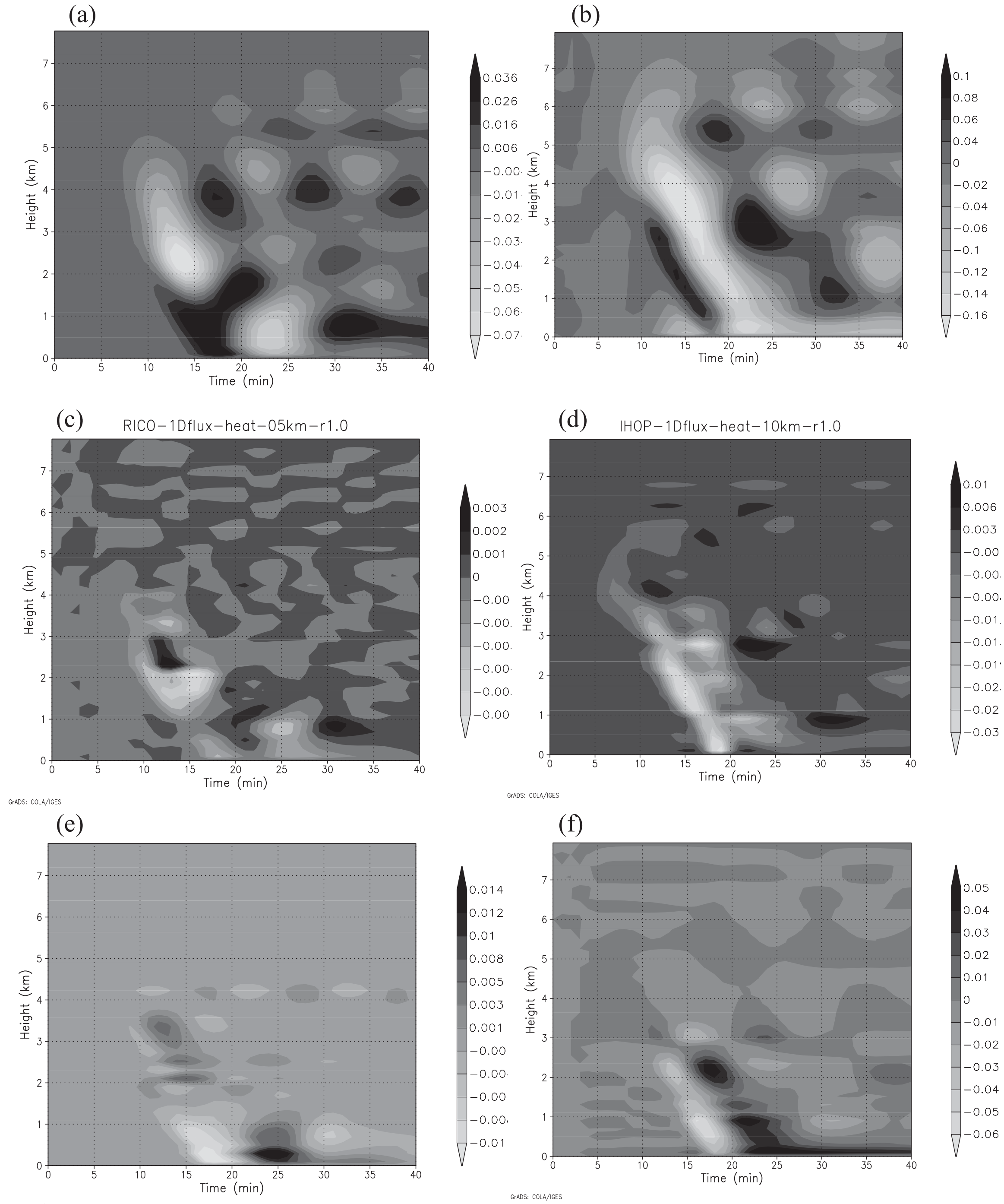

Fig. 17. The differences of simulated (a) mass ($\times 10^8$ kg s^{-1}), (c) heat ($\times 10^{12}$ J s^{-1}), and (e) moisture ($\times 10^6$ kg s^{-1}) fluxes between ER95R1 and ER95 (i.e., ER95R1–ER95) for the RICO case with the 5-km bubble size; (b), (d), and (f) are the same as (a), (c), (e), respectively, except for the IHOP case with the 10-km bubble size. Note that different color scales are used in different figures.

tive clouds, under larger bubble sizes and the maximum vertical velocity was capped when the bubble radius was larger than 3 km. For IHOP, each simulation produced only one convective cloud and the maximum vertical velocity and the cloud life cycle increased when the bubble size increased (Fig. 3b). The simulated 3D cloud base was almost independent of the bubble size, while the 3D cloud top developed higher when a larger bubble was used for both cases.

1D ETTM cloud simulations corresponding to each of the WRF simulations were conducted. The cloud radius and the tilting angle required in ETTM were estimated from 3D WRF cloud simulations and will be parameterized using grid-scale information in the future. Compared with the 3D clouds, results from ETTM were too weak for the original thermal bubbles for all cloud parameters: the vertical velocity was too weak; the cloud depth was too shallow, etc. While the 3D clouds took time to develop, the 1D clouds developed right after ETTM integration. This is because a moistening process at the low levels before the 3D clouds developed was missing in 1D cloud development.

To compensate for the missing moistening process, two sensitivity experiments, which imposed a lower bound of relative humidities of 88% (ER88) and 95% (ER95) in the thermal bubble of the updraft, were carried out. After adding extra moisture into the thermal bubble, the simulated 1D updraft developed stronger (i.e., a larger vertical velocity) and deeper, though the depth was still underestimated. In particular for IHOP, larger clouds were able to penetrate the inversion at a 3–4 km height (Fig. 2b), which capped the development of the 1D cloud with the original thermal bubble (i.e., without extra moisture). For ER95, when compared with 3D cloud results, the depth of the vertical mass, heat, and moisture flux distribution was too shallow; the erroneous negative mass fluxes were caused by ETTM downdraft; and the life expansion of the 1D cloud from IHOP was too short. Overall, the simulated 1D cloud results for IHOP were slightly worse than those for RICO, and this might be because the environment sounding from IHOP was more sophisticated than that from RICO. Note that, in addition to the moistening process, there are other important terms that are omitted in ETTM, such as the horizontal transport, wind shear, density current, etc., which also tend to degrade ETTM performance.

Sensitivity tests with a zero-degree tilting angle (i.e., ER95A0) or with the ratio of the downdraft radius to the updraft radius equal to 1 (i.e., ER95R1) were carried out for ER95 simulations. Results show that for these two case studies, the downdraft due to the tilting of the cloud was able to slightly improve ETTM's performance, including the increase in the heat and moisture fluxes in the lower to middle atmosphere, except for the heat flux from RICO. For the test with a larger downdraft size, the reduction in the upward mass flux due to the downdraft became more pronounced, except for low levels when a smaller bubble size was used. However, after the use of a larger downdraft size, the upward heat flux due to the downdraft became weaker and the variation in the total moisture flux during the cloud life cycle was much smaller than that due to the sensitivity test of the tilting angle mentioned above. Overall, the influence of using different downdraft sizes on simulated 1D cloud results is not clear, and more studies will be needed in the future.

It is very unlikely that 1D ETTM can fully reproduce 3D cloud features. The addition of moisture to the thermal bubble, which is a reasonable approach, clearly improved ETTM performance. Although there were discrepancies between ER95 and the WRF simulation, the overall patterns of mass, heat, and moisture fluxes from both models were somewhat similar. This is quite promising and when ETTM is used in cumulus parameterization in the future, a relative humidity of 95% will be imposed into the thermal bubble for initial testing. It is understood that, besides the moisture, there are other factors that can cause an underestimation of the cloud depth, and more improvements are required in order to enhance ETTM performance. More importantly, a comparison with high-resolution observations, such as radar data, is required to further assess and improve ETTM performance.

Acknowledgements

The authors would like to acknowledge the WRF model development teams for their efforts on model development. We would also like to thank Dr. Teruyuki Kato, the editor of this manuscript, and two anonymous reviewers for their valuable scientific comments on the manuscript. This work was supported by a National Science Council grant #95-2111-M-008-040 in Taiwan.

References

Anthes, R. A., 1977: A cumulus parameterization scheme utilizing a one-dimensional cloud model. *Mon. Wea. Rev.*, **105**, 270–286.

Arakawa, A., 1969: Parameterization of cumulus clouds. *Proc. Symp. on Numerical Weather Prediction*, Tokyo, Japan, WMO/International Union of Geodesy and Geophysics, 1–6.

Arakawa, A., 2004: The cumulus parameterization problem: past, present, and future. *J. Climate*, **17**, 2493–2525.

Brown, J. M., 1979: Mesoscale unsaturated downdrafts driven by rainfall evaporation: A numerical study. *J. Atmos. Sci.*, **36**, 313–338.

Chen, S.-H., and W.-Y. Sun, 2002: A one-dimensional time-dependent cloud model. *J. Meteor. Soc. Japan*, **80**, 99–118.

Chen, S.-H., and W.-Y. Sun, 2004: An explicit one-dimensional time-dependent tilting cloud model. *J. Atmos. Sci.*, **61**, 2797–2816.

Cheng, M.-D., 1989: Effects of downdrafts and mesoscale convective organization on the heat and moisture budgets of tropical cloud clusters. Part II: Effects of convective downdrafts. *J. Atmos. Sci.*, **46**, 1540–1564.

Ferrier, B. S., and R. A. Houze, 1989: One-dimensional time-dependent modeling of GATE cumulonimbus convection. *J. Atmos. Sci.*, **46**, 330–352.

Frank, W. M., and C. Cohen, 1985: Properties of tropical cloud ensembles estimated using a cloud model and an observed updraft population. *J. Atmos. Sci.*, **42**, 1911–1928.

Fritsch, J. M., and C. F. Chappell, 1980: Numerical prediction of convectively driven mesoscale pressure systems. Part I: Convective parameterization. *J. Atmos. Sci.*, **37**, 1722–1733.

Gao, S., and X. Li, 2008: Impacts of initial conditions on cloud-resolving model simulations. *Adv. Atmos. Sci.*, **25**, 737–747.

Grabowski, W. W., 2001: Coupling cloud processes with the large-scale dynamics using the cloud-resolving convection parameterization. *J. Atmos. Sci.*, **58**, 978–997.

Gray, M. E. B., 2000: Characteristics of numerically simulated mesoscale convective systems and their application to parameterization. *J. Atmos. Sci.*, **57**, 3953–3970.

Grell, G. A., Y.-H. Kuo, and R. J. Pasch, 1991: Semi-prognostic tests of cumulus parameterization schemes in the middle latitudes. *Mon. Wea. Rev.*, **119**, 5–31.

Grell, G. A., 1993: Prognostic evaluation of assumptions used by cumulus parameterizations. *Mon. Wea. Rev.*, **121**, 764–787.

Haines, P. A., and W. Y. Sun, 1994: A convective cloud model for use in a cumulus parameterization scheme. *Mon. Wea. Rev.*, **122**, 165–182.

Hu, Qi, 1997: A cumulus parameterization based on a cloud model of intermittently rising thermals. *J. Atmos. Sci.*, **54**, 2292–2307.

Kain, J. S., and J. M. Fritsch, 1990: A one-dimensional entraining/detaining plume model and its application in convective parameterization. *J. Atmos. Sci.*, **47**, 2784–2802.

Kain, J. S., and J. M. Fritsch, 1993: *Convective parameterization for mesoscale models: The Kain-Fritsch scheme. Meteor. Monogr.*, No. **46**, Amer. Meteor. Soc., 165–170.

Khairoutdinov, M. F., D. A. Randall, and C. A. DeMott, 2005: Simulations of the atmospheric general circulation using a cloud-resolving model as a superparameterization of physical processes. *J. Atmos. Sci.*, **62**, 2136–2154.

Khairoutdinov, M. F., C. A. DeMott, and D. A. Randall, 2008: Evaluation of the simulated interannual and subseasonal variability in an AMIP-style simulation using the CSU Multiscale Modeling Framework. *J. Climate*, **21**, 413–431.

Klemp, J. B., and R. B. Wilhelmson, 1978: Simulations of right- and left-moving storms produced through storm splitting. *J. Atmos. Sci.*, **35**, 1097–1110.

Kuo, H. L., 1974: Further studies of the parameterization of the influence of cumulus convection on large-scale flow. *J. Atmos. Sci.*, **31**, 1232–1240.

Lemone, M. A., and E. J. Zipser, 1980: A quasi-one-dimensional cumulus cloud model and parameterization of cumulus heating and mixing effects. *Mon. Wea. Rev.*, **108**, 991–1009.

Lin, C., 1999: Some bulk properties of cumulus ensembles simulated by a cloud-resolving model. Part I: Cloud root properties. *J. Atmos. Sci.*, **21**, 3724–3735.

Liu, C., M. W. Moncrieff, and W. W. Grabowski, 2001: Explicit and parameterized realizations of convective cloud systems in TOGA COARE. *Mon. Wea. Rev.*, **129**, 1689–1703.

Luo, Y., K.-M. Xu, H. Morrison, G. M. McFarquhar, Z. Wang, and G. Zhang, 2008: Multi-layer arctic mixed-phase clouds simulated by a cloud-resolving model: Comparison with ARM observations and sensitivity experiments. *J. Geophys. Res.*, **113**, doi:10.1029/2007JD009563.

Manabe, S., J. Smagorinsky, and R. F. Strickler, 1965: Simulated climatology of a general circulation model with a hydrological cycle. *Mon. Wea. Rev.*, **93**, 769–798.

Molinari, J., and T. Corsetti, 1985: Incorporation of cloud-scale and mesoscale downdrafts into a cumulus parameterization: Results of one- and three-dimensional integrations. *Mon. Wea. Rev.*, **113**, 485–501.

Moncrieff, M. W., 1981: A theory of organized steady convection and its transport properties. *Quart. J.*

Roy. Meteor. Soc., **107**, 29–50.

Moncrieff, M. W., 1992: Organized convective systems: Archetypal dynamical models, mass and momentum flux theory, and parameterization. *Quart. J. Roy. Meteor. Soc.*, **118**, 819–850.

Murata, A., and M. Ueno, 2005: The vertical profile of entrainment rate simulated by a cloud-resolving model and application to a cumulus parameterization. *J. Meteor. Soc. Japan*, **83**, 745–770.

Schlesinger, R. E., 1978: A three-dimensional numerical model of an isolated thunderstorm: Part I. Comparative experiments for variable ambient wind shear. *J. Atmos. Sci.*, **35**, 690–713.

Skamarock, W., J. Klemp, J. Dudhia, D. Gill, D. Barker, W. Wang, and J. Powers, 2005: *A description of the Advanced Research WRF version 2*. NCAR Technical note. 100 pp.

Smagorinsky, J., 1963: General circulation experiments with the primitive equations. I. The basic experiment. *Mon. Wea. Rev.*, **91**, 99–164.

Sun, W. Y., 1984: Numerical analysis for hydrostatic and nonhydrostatic equations of inertial-internal gravity waves. *Mon. Wea. Rev.*, **112**, 259–268.

Sun, W. Y., and P. A. Haines, 1996: Semi-prognostic tests of a new mesoscale cumulus parameterization scheme. *Tellus*, **48A**, 272–289.

Tao, W.-K., J.-D. Chern, R. Atlas, D. Randall, M. Khairoutdinov, J.-L. Li, D. E. Waliser, A. Hou, X. Lin, C. Peters-Lidard, W. Lau, J. Jiang, and J. Simpson, 2009: A multi-scale modeling system: Developments, applications and critical issues. *Bull. Amer. Meteor. Soc.*, **90**, 515–534.

Tao, W.-K., J. R. Scala, B. Ferrier, and J. Simpson, 1995: The effect of melting processes on the development of a tropical and a midlatitude squall line. *J. Atmos. Sci.*, **11**, 1934–1948.